The Astrophysical Journal, 648:250–267, 2006 September 1

THE BRIGHT AGES SURVEY. II. EVOLUTION OF LUMINOSITY, DUST EXTINCTION, AND STAR FORMATION FROM $z = 0.5$ TO $z = 2.5$[1]

James W. Colbert
Spitzer Science Center, California Institute of Technology, Pasadena, CA 91125

and

Matthew A. Malkan and R. Michael Rich
University of California, Los Angeles, CA, 90095
Received 2005 October 14; accepted 2006 May 8

ABSTRACT

The Bright Ages Survey is a *K*-band–selected redshift survey over six separate fields with *UBVRIzJHK* imaging covering a total of 75.6 arcmin^2 and reaching $K = 20$–20.5. Two fields have deep *HST* imaging, while all are centered on possible overdensities in the $z \sim 2$ range. Here we report photometric redshifts and spectroscopy for this sample, which has been described in Paper I. We find 18 galaxies with spectroscopic redshifts of $z > 1.5$. The derived rest-frame *R*-band luminosity functions show strong evolution out to $z = 2$. The luminosity function at $z = 2$ shows more bright galaxies than at any other epoch, even the extrapolated $z = 3$ luminosity function from Shapley et al. However, the *R*-band integrated luminosity density remains roughly constant from to $z = 0.5$ to $z = 2$. Evolved galaxies (E, S0, Sa) show a decreasing contribution to the total *R*-band luminosity density with redshift. The dust extinction in our *K*-selected sample is moderately larger [median $z = 2$ $E(B - V) = 0.30$] than that found in Lyman break galaxies, although not enough to make a significant impact on the total light or star formation found at high redshift. We measure the extinction-corrected star formation rate density at $z = 2$, finding $\rho_{\rm SFR}(z = 1.5$–$2.5) = 0.093\ M_\odot\ {\rm yr}^{-1}\ {\rm Mpc}^{-3}$, consistent with a relatively flat instantaneous star formation rate from $z = 1$–4.

Subject headings: galaxies: evolution

Online material: machine-readable table

1. INTRODUCTION

While galaxy searches are now beginning to push out as far as $z = 6$ (e.g., Giavalisco et al. 2004), it is the more intermediate-redshift ranges that appear to be the epochs during which the familiar components of modern galaxies assembled. The redshift range $z = 1$–2.5 spans about 25% of age of the universe (3 Gyr), more than that covered from $z = 2.5$ to the big bang. The integrated luminosity density and global star formation rates appear to increase with redshift out to $z = 1$, before leveling off out to around $z \sim 4$, with a possible slight fall to $z = 6$ (Lilly et al. 1996; Steidel et al. 1999; Giavalisco et al. 2004). It is this combination of sustained peak star formation rate and length of cosmic time that makes the range $z = 1$–2.5 the "Bright Ages" of the universe: the epoch when most stars, and presumably heavy elements, formed.

As the Bright Ages commence near redshift $z \approx 2.5$, much of the galaxy population appears irregular (Giavalisco et al. 1996) with many diffuse and asymmetric star-forming galaxies (Conselice et al. 2004), although a handful of massive galaxies appear to be in place (Cimatti et al. 2004). By the end of the Bright Ages at $z = 1$, much of the familiar character of the present-day universe is in place: most galaxies can be classified on the traditional Hubble sequence, and rich clusters of galaxies are found. This redshift range is increasingly being found to host some of the most interesting phenomena that may be related to the formation of the precursors of present-day massive galaxies and clusters. These include the classes of extremely red objects (EROs; Cimatti et al. 2002a; Firth et al. 2002), submillimeter galaxies (Chapman et al. 2005), and large-scale structures (e.g., Pascarelle et al. 1998; Campos et al. 1999; Palunas et al. 2004).

The near-infrared is essential for a robust study of the Bright Ages. Most high-redshift surveys are based on visible wavelengths, where targets at high redshift are selected using rest-frame blue or UV light, creating a strong bias against the discovery of red galaxies. Deep near-infrared–selected surveys, like the Las Campanas Infrared Survey (McCarthy et al. 2001), K20 Survey (Cimatti et al. 2002b), and FIRES (Faint Infrared Extragalactic Survey; Franx et al. 2000), find substantial numbers of red galaxies that would be missed by optical surveys. Rest-frame optical is also a better tracer of the stellar mass for high-redshift galaxies than rest-frame ultraviolet, which can be dominated by recent starbursts, even if only a small percentage of the total galactic mass is involved (i.e., Shapley et al. 2005). Near-infrared photometry is critical for robust template fitting at these redshifts. The 4000 Å Balmer break is one of the strongest galaxy spectral features and can be used to estimate both redshift and age (i.e., Franx et al. 2003; Förster Schreiber et al. 2004). In particular, to reach $z = 2.5$ requires good photometry in the *K* filter, so that at least one point in the spectral energy distribution is cleanly on the *red* side of the Balmer break.

Ultraviolet luminosity is a poor estimator of star formation rate for the highest luminosity sources (Martin et al. 2005), saturating around $10^{10}\ L_\odot$ as dust extinction reprocesses a larger fraction of the emitted radiation into the infrared (Spinoglio et al. 1995; Malkan & Stecker 2001). Any correction to even moderate

[1] The data presented herein were obtained at the W. M. Keck Observatory, which is operated as a scientific partnership among the California Institute of Technology, the University of California and the National Aeronautics and Space Administration. The Observatory was made possible by the generous financial support of the W. M. Keck Foundation.

star formation determined from ultraviolet flux can be highly uncertain, ranging from factors of 2–10 (Calzetti 1997; Dickinson 1998; Tresse & Maddox 1998). Luminous galaxies dominate the star formation rate density at $z = 1$ (Elbaz et al. 2002), potentially pointing to a serious underestimation of star formation by ultraviolet sensitive surveys out to the highest redshifts. For example, the SWIRE (*Spitzer* Wide-Area Infrared Extragalactic) survey is finding more Arp 220–like ultraluminous infrared galaxies (ULIRGs) than suggested by previous count models out to at least $z = 1.5$ (Rowan-Robinson et al. 2005). However, studies of Lyman break galaxies at $z = 2$–4 show little evidence for significant dust extinction [average $E(B - V) \sim 0.15$] (Steidel et al. 1999; Adelberger & Steidel 2000), even when including much longer wavelength 3.5–8 μm data (Barmby et al. 2004). The danger remains that this may be a selection effect, as analysis of deep near-infrared–selected $J - K$ galaxies (Labbé et al. 2005) and SCUBA sources (Smail et al. 2002) indicate significant quantities of high-redshift dust-extincted star formation.

The local optical luminosity function is known to relatively high precision (Cross et al. 2001; Blanton et al. 2001). Measurements of luminosity density show significant evolution out to $z = 1$ (i.e., Lilly et al. 1996; Cohen et al. 2000), consistent with a steady brightening of the typical galaxy luminosity. This trend appears to continue to the highest redshifts ($z \sim 3$) where the luminosity functions are dramatically brighter than those seen locally (Shapley et al. 2001). Near-infrared studies of the galaxy luminosity function have generally been consistent with the predictions of pure luminosity evolution (PLE). Kashikawa et al. (2003), for instance, found their K-band luminosity functions to be consistent with PLE out as far as $z = 3$. Over a narrower redshift range, $z = 0.5$–1.5, the Las Campanas Infrared Survey (Chen et al. 2003) finds evolution in their H-band–selected sample to be so mild that it is consistent with no evolution altogether. While not necessarily contradictory, results such as these clearly demonstrate that there remains significant uncertainty in our understanding of $z > 1$ galaxy evolution.

Blue and red galaxy luminosity functions also appear to evolve differently (Lilly et al. 1995). There is some evidence for number density evolution for late-type galaxies (Lin et al. 1999), although this increase in blue galaxies with redshift is not seen in all studies (i.e., Cohen 2002). Red galaxies show little change in K-band number density out to $z = 1$ ($\sim$30%, K20 Survey; Pozzetti et al. 2003), although this appears to change at the highest redshifts. Rest-frame optical luminosity functions from out to $z = 3$ show a clear bifurcation between blue and red galaxies, with early-type galaxies showing an order of magnitude drop in both number and luminosity density (Giallongo et al. 2005). A near-infrared sample is essential to ensure the inclusion of these red, early-type galaxies.

We survey a total of 75.6 arcmin^2 in six fields dispersed across the sky. The total area is comparable to the 52 arcmin^2 of the similarly deep K20 survey. The K20 survey acquired a more complete spectroscopic sample, but the larger number of widely separated fields in our survey might be expected to better mitigate against cosmic variance.

Here we present the second paper in a series of papers on the Bright Ages survey. Paper I (Colbert et al. 2006) presents a K-selected sample and its accompanying multiband *UBVRIzJH* photometry and ERO density. In this paper we present the multislit spectroscopic follow-up of a subset of the Bright Ages sample and compare that to photometric redshifts, providing a measurement of their reliability. We then use the photometric redshifts on the entire sample to derive dust extinctions, luminosity functions and star formation rates out to the $z = 2$ universe. Unless otherwise stated, the assumed cosmology is an $\Omega_M = 0.3$, $\Omega_\Lambda = 0.7$ universe with a $H_0 = 70$ km s^{-1} Mpc^{-1}.

2. OPTICAL MULTISLIT LRIS SPECTROSCOPY

All spectroscopy was done at the W. M. Keck Observatory using the Low Resolution Imaging Spectrometer (LRIS; Oke et al. 1995) over eight nights from 2000 March through 2003 August. The initial two-night run took place before the introduction of the blue-sensitive LRIS-B camera, but all subsequent spectroscopy data were obtained with both the red and blue LRIS cameras simultaneously. The cameras and their CCDs are described in Paper I. For the first two nights of observations with the red-sensitive LRIS-R camera, the GG495 long-pass order-blocking filter was used to remove any contaminating light below 4950 Å, but all subsequent observations (2002 June onward) employed the dichroic beam splitter, which acted as an order blocking filter. We used either the 560 or the 680 dichroic, splitting the light at 5600 and 6800 Å, respectively.

For most LRIS-R spectroscopy we used the 400 g mm^{-1} grating (1.86 Å pixel^{-1}, covering 3800 Å), although on a few nights we used the 600 g mm^{-1} grating (1.28 Å pixel^{-1}, covering 2620 Å) instead. The central wavelength for the LRIS-R coverage ranged from 7000 to 8100 Å. For the short wavelength camera (LRIS-B) we used three different grisms: 300, 400, and 600 l mm^{-1}, with corresponding dispersions of 1.43, 1.09, and 0.63 Å pixel^{-1} and wavelength coverages of 2210–8060, 1760–6220, and 3300–5880 Å. In practice, the low-wavelength limit for all grisms was $\sim$3500 Å. A summary of observations, integration times, dichroics, gratings, grisms, slit masks, and number of spectra taken are presented in Table 1.

All spectroscopy, except for the calibration stars, was done using multislits. All fields were registered to the star positions from the United States Naval Observatory Flagstaff Station (USNOFS) catalog. Each slit was 1″–1.″4 wide and at least 6″ long, although usually closer to 10″ in length except in areas of highest target concentration. A typical slit mask held 21–22 slits for targets, but for most fields only a fraction targeted the primary K-selected sample, as the near-infrared images were typically significantly smaller than the LRIS field of view. A total of 24 slit masks were used. We observed each slit mask for an integration time ranging from 68 to 160 minutes, with $\sim$100 minutes being typical. Observations were taken at two different dither positions along the slits, separated by 2″–3″, depending on seeing. Each integration at each dither position ranged from 1800 to 2580 s.

We reduced the data using standard software tools in IRAF and its NOAO ONEDSPEC and TWODSPEC packages. The two dither positions are subtracted from each other, which removes the bias and the majority of sky and skyline flux, although not perfectly, as the skylines vary even on the timescale of minutes. Each slit-mask image is divided by its flat field and cut into a final two-dimensional spectral image for each slit. The exception to this method were any slits with objects so close together that their dithered spectra overlapped. In these cases, the final two-dimensional spectral images were produced without the dithered subtraction. This left all the sky flux and skylines still to be removed, but was the only choice for producing an uncontaminated spectrum.

Flat-fielding was done either using spectroscopic dome light reflected off the interior of the Keck I dome or, in the case of 2003 August LRIS-B, twilight sky flats. A calibration star spectrum is taken in the single long-slit mode, either at the beginning or the end of each night for use as a flux calibrator. While not a highly accurate method of flux calibration (each slit illuminates a different part of the detector, covers different wavelength ranges,

TABLE 1
JOURNAL OF OBSERVATIONS FOR LRIS SPECTROSCOPY

Target Field	No. of Spectral Redshifts	Integration[a] Time (s)	Dichroic	Grating (g mm^{-1})	Grism/Central λ (l mm^{-1} Å)	No. of Slit Masks	Observation Date
0149+336	12	7200	560	600	400/7250	1	2003 Feb 25
0741+652	7	12450	560	600	400/7250	2	2003 Feb 25
0953+549	15	15600	560	600	400/7250	2	2003 Jan 4
		6090	560	600	400/7250	1	2003 Mar 25
1107+7239	24	33800	None	None	600/7000	5	2000 Mar 1–2
		10250	560	600	400/7250	2	2003 Feb 25
2359+068	33	5400	560	600	400/7250	1	2003 Jan 4
		11580	680	300	600/8100	2	2003 Aug 28–29
1714+5015	79	16800	560	400	400/7500	3	2002 Jun 11
		11250	560	600	400/7250	2	2003 Mar 25
		18300	680	300	600/8100	3	2003 Aug 28–29

[a] Integration times given for LRIS-B side, unless only LRIS-R was available. LRIS-R integration times ranged from equal to 5% less, due to a slower CCD read-out.

allows different amounts of light through from different-sized target images, etc.), it provides a reasonable estimate of the flux at each wavelength: ~30% accurate as determined from comparisons to broadband photometry.

All wavelength calibration was done using either a set of Hg, Cd, Ne, and Ar standard arcs done immediately after the observation of a slit mask was completed, or from the night skylines. Both were used interchangeably, depending on the quality of the standard arcs, and both generally produced wavelength accuracies good to ~1 Å. After wavelength calibration the spectra were flux-calibrated to a spectroscopic standard taken on the same night and then clipped of low signal-to-noise wavelength regions at the extremes.

The one-dimensional spectrum extraction aperture size for each night ranged from 1.″5 to 1.″9 depending on seeing and some sample extractions of data. In some cases, particularly those spectra that had not been dithered-subtracted, a clear skyline signal still remained in the data, usually a distinctive positive/negative trough and peak shape, presumably a result of the median background actually being slightly offset from the actual background at the position of the spectra. By taking the extracted sky used in the initial subtraction, shifting it one pixel, inverting it and subtracting it from itself a similar positive/negative pattern can be created. This final background was shifted, scaled, and subtracted from the data in such a way as to minimize the rms of the night skyline regions. This was only done for the long-wavelength data, and only for about 10% of that. In those cases, the improvement in final rms of the sky line regions was typically only 10%–20%, although in a few instances the effect was dramatic, reducing the remaining skyline signal by factors of 2–3.

2.1. *Spectroscopic Redshift Results*

Targets for spectroscopic follow-up were chosen primarily on the basis of photometric redshifts (see below) indicating that they are at $z > 1$, with priority given to those with $z > 1.5$. Secondary priority was given to targets with red optical to near-infrared colors, mostly EROs ($R - K > 5$), although some red targets with less extreme $R - K$ color were also targeted. We filled the remaining slits in the slit mask with any near-infrared sources that were available. As we continued to acquire new photometry through 2003, repeated observations of the same fields often used different, updated photometric redshifts and colors for selection.

We took spectra of 310 *K*-selected targets. Of those, 70 had spectra too faint to extract, while an additional 70 had either no features or features so weak as to make their identification uncertain. Many of these are presumably in the "redshift desert" around $z \sim 1.5$, where no strong spectral features fall anywhere in the optical. An additional 24 of the *K*-selected spectra are identified as stars: mostly dim, red K and M stars. We present a list of all sources with successful spectroscopic redshifts in Table 2. The relatively low successful galaxy spectroscopic identification rate (146 of 310, or ~47%) can mainly be attributed to the target selection. The near-infrared targets were selected primarily on the basis of extreme red color and photometric redshifts indicating a high z, without regard to their optical fluxes. Bluer, lower redshift sources were chosen as secondary targets. In other words, the spectroscopic follow-up was biased toward the faintest red sources with the greatest intrinsic interest, but the lowest probability of spectral identification.

All spectra were processed through the IRAF program `xcsao`, which computes a redshift by cross-correlating each spectrum with a set of galaxy templates. For templates we used a set of UV–optical spectra made by averaging galaxies from the catalog of Storchi-Bergmann et al. (1998). In addition to these elliptical, spiral, and starburst templates, we also used a composite spectra of ~1000 Lyman break galaxies (Shapley et al. 2003) to explore the highest redshifts and the bluest rest wavelengths. In cases where `xcsao` failed to give a good cross-correlation, we examined the spectrum with a detailed line list to find features and identify redshift. Finally, the two-dimensional spectra were closely examined in all cases. A faint emission line, while often ambiguous in the final one-dimensional spectrum, gives a distinctive positive/negative signal in the two-dimensional image, from the differencing of the two dithered spectra. Spectra of all 18 $z > 1.5$ galaxies are displayed in Figure 1, while the overall spectroscopic redshift distribution is plotted in Figure 2. We note that there is no significant continuum detection for source 1714 M170, particularly blueward of the line (a slight hint of continuum is visible redward in two-dimensional image). The offset from zero is a result of an imperfect sky subtraction. By way of comparison, out of 459 spectroscopic redshifts, the K20 survey reports 22 galaxies (excluding Type I active galactic nuclei [AGNs]) with confirmed redshifts of $z > 1.5$–3 (Cimatti et al. 2002c).[2]

Plotting $R - I$ versus $J - K$ colors (Fig. 3), we find that ~85% $K < 20$ stars clearly segregate from the galaxy and AGN population, with $R - I > 0.65$ and $J - K < 1.0$. This cut is mostly in $J - K$, which is blue for cool dwarf stars in the range of 3000 K (Bessell et al. 1998). In our spectroscopically observed sample this results in only a single extremely red $z = 0.688$ galaxy being removed from the sample. Near-infrared colors evolve rapidly

[2] See also http://www.arcetri.astro.it/~k20.

TABLE 2

SPECTROSCOPIC IDENTIFICATIONS OF NEAR-INFRARED SOURCES

Field	R.A. (J2000.0)	Decl. (J2000.0)	Name	K Magnitude	$R-K$	Spectroscopic z	Quality[a]	Comments
0149+336	01 52 15.89	33 49 52.8	S52	18.20	n/a	0.443	3	
0149+336	01 52 22.80	33 49 14.0	S22	19.80	2.45	0.282	3	
0149+336	01 52 28.75	33 51 25.3	M59	19.31	3.49	0.657	3	
0149+336	01 52 29.75	33 51 23.6	M52	18.33	4.70	1.121	3	
0149+336	01 52 30.97	33 49 47.6	S15	19.33	1.90	3.993	3	BL AGN
0149+336	01 52 36.59	33 49 18.5	S6	19.32	>4.67	2.341	2	
0741+652	07 41 26.99	65 15 25.0	A71	20.71	2.70	0.479	2	
0741+652	07 41 33.90	65 15 16.8	A62	17.98	1.22	1.44	3	AGN
0741+652	07 41 34.95	65 14 14.6	A19	20.67	4.43	0.816	1	
0741+652	07 41 41.28	65 14 58.9	A47	19.91	2.11	0.268	3	
0741+652	07 41 43.82	65 14 39.8	A36	19.82	3.14	0.746	1	
0741+652	07 41 44.40	65 13 56.5	A6	20.85	3.84	0.87	1	
0741+652	07 41 48.84	65 15 51.3	A84	19.69	4.80	0.83	1	
0953+549	09 57 05.72	54 42 52.3	N19	20.13	4.83	0.436	3	
0953+549	09 57 07.20	54 40 00.0	S59	19.68	3.95	1.463	2	AGN
0953+549	09 57 07.51	54 40 02.8	S63	17.82	6.19	1.088	1	
0953+549	09 57 07.72	54:41 21.4	N54	18.65	3.26	0.571	3	
0953+549	09 57 08.81	54 42 28.3	N32	17.33	4.68	2.32	3	
0953+549	09 57 08.92	54 41 05.6	N62	18.91	3.69	0.623	2	
0953+549	09 57 12.54	54 37 57.6	S9	18.23	4.13	0.727	3	
0953+549	09 57 12.63	54 42 23.0	N41	18.11	4.19	0.726	2	
0953+549	09 57 13.92	54 43 03.3	N16	19.76	3.30	0.602	2	
0953+549	09 57 14.56	54 37 55.0	S14	19.89	2.67	0.391	3	
0953+549	09 57 15.49	54 39 03.8	S41	19.70	2.96	1.059	2	
0953+549	09 57:15.70	54 38 06.5	S15	19.13	2.90	0.688	3	
0953+549	09 57 18.43	54 37 59.7	S12	18.59	2.47	0.252	3	
0953+549	09 57 20.32	54 39 09.0	S43	20.01	3.75	0.782	2	
0953+549	09 57 20.47	54 37 33.4	S1	19.23	2.85	0.688	3	
1107+7239	11 06 34.08	72 37 53.1	M42	19.87	3.93	0.661	1	
1107+7239	11 06 36.47	72 39 02.2	M32	20.28	3.71	2.95	2	
1107+7239	11 06:39.21	72 39 40.2	M25	17.87	3.94	0.569	3	
1107+7239	11 06 40.63	72 38 48.7	A43	17.22	5.02	0.776	2	
1107+7239	11 06 46.41	72 38 59.2	A35	16.65	3.59	0.426	3	
1107+7239	11 06 49.67	72 39 03.2	A32	18.17	4.57	0.743	2	
1107+7239	11 06 53.59	72 39 54.2	A28	20.11	3.20	0.468	2	
1107+7239	11 06 53.82	72 38 42.3	A25	17.60	4.04	0.474	2	
1107+7239	11 06 53.91	72 40 06.4	A24	18.94	3.29	0.462	3	
1107+7239	11 06 54.36	72 38 01.0	M19	19.39	5.48	0.723	2	
1107+7239	11 06 54.72	72 38 56.7	A22	18.18	5.46	1.214	1	
1107+7239	11 06 54.96	72 37 55.8	M18	18.37	4.38	0.717	2	
1107+7239	11 06 56.62	72 39 35.2	A19	17.56	4.23	0.887	3	
1107+7239	11 06 58.22	72 39 23.7	A15	18.16	3.32	0.421	2	
1107+7239	11 06 58.25	72 39 50.0	A13	18.64	5.58	1.203	1	
1107+7239	11 07 03.77	72 40 20.5	A4	17.82	3.89	0.328	2	
1107+7239	11 07 03.82	72 39 30.1	A5	19.63	2.91	0.61	2	
1107+7239	11 07 07.08	72 39 11.7	A2	19.19	4.36	0.771	3	
1107+7239	11 07 07.47	72 39 22.7	A1	17.94	3.96	0.609	3	
1714+5015	17 14 05.68	50 15 27.2	S48	16.97	3.78	0.387	3	
1714+5015	17 14 06.02	50 17 47.7	S68	19.17	4.04	0.927	2	
1714+5015	17 14 06.49	50 17 40.0	S71	19.86	3.39	0.184	3	
1714+5015	17 14 06.73	50 14 25.3	S23	18.31	5.70	1.044	2	
1714+5015	17 14 07.30	50 15 35.6	S45	18.27	3.83	0.681	3	
1714+5015	17 14 07.58	50 16 55.9	S93	19.88	4.49	0.598	3	
1714+5015	17 14 08.66	50 18 17.1	S40	18.13	3.12	0.186	3	
1714+5015	17 14 09.50	50 17 55.6	M134	19.30	2.47	0.184	3	
1714+5015	17 14 09.53	50 15 49.5	M93	18.28	4.07	0.538	3	
1714+5015	17 14 09.74	50 15 34.2	M102	19.85	3.14	0.898	3	
1714+5015	17 14 09.88	50 14 04.2	M20	20.26	4.23	1.045	1	
1714+5015	17 14 10.39	50 14 38.5	M36	19.17	3.49	2.083	3	BL AGN
1714+5015	17 14 10.61	50 18 23.7	M51	18.84	3.13	0.529	3	
1714+5015	17 14 11.17	50 14 44.9	M37	18.11	4.75	0.772	2	
1714+5015	17 14 11.26	50 17 05.0	M168	18.18	6.20	1.027	2	
1714+5015	17 14 11.27	50 13 50.1	M10	19.96	3.56	0.776	3	
1714+5015	17 14 11.32	50 14 10.9	M21	18.15	5.51	0.93	2	

TABLE 2—*Continued*

Field	R.A. (J2000.0)	Decl. (J2000.0)	Name	K Magnitude	$R-K$	Spectroscopic z	Quality[a]	Comments
1714+5015	17 14 11.35	50 16 10.1	M82	18.48	3.75	2.398	3	BL AGN; Object 19[b]
1714+5015	17 14 11.92	50 17 06.7	M162	20.08	2.67	0.257	3	
1714+5015	17 14 11.94	50 14 46.1	M42	20.35	2.70	0.568	3	
1714+5015	17 14 11.94	50 16 01.9	M89	19.27	4.38	2.391	3	AGN; Object 18[b]
1714+5015	17 14 12.37	50 17 32.4	M147	17.68	4.03	0.568	2	
1714+5015	17 14 12.43	50 17 25.3	M160	18.20	2.82	0.311	3	
1714+5015	17 14 12.44	50 18 19.0	M129	19.90	3.93	2.40	3	BL AGN
1714+5015	17 14 12.68	50 14 33.3	M32	18.26	3.11	0.275	3	
1714+5015	17 14 12.83	50 17 50.8	M148	19.94	2.51	0.311	3	
1714+5015	17 14 13.72	50 16 51.2	M48	19.51	4.58	1.03	2	
1714+5015	17 14 13.73	50 16 09.8	M85	20.64	2.55	0.221	1	
1714+5015	17 14 13.91	50 17 33.9	M150	18.59	3.00	0.531	3	
1714+5015	17 14 14.28	50 17 51.0	M142	18.77	5.83	0.803	1	
1714+5015	17 14 14.54	50 18 23.5	M52	19.28	4.38	1.088	2	
1714+5015	17 14 14.73	50 17 06.8	M165	19.08	4.06	1.207	2	
1714+5015	17 14 14.77	50 15 30.4	M107	18.39	4.25	2.387	3	AGN; 53w002
1714+5015	17 14 15.00	50 16 52.1	M173	19.87	2.37	0.046	3	
1714+5015	17 14 15.06	50 17 19.9	M163	20.61	3.85	0.247	3	
1714+5015	17 14 15.33	50 17 15.7	M65	18.81	5.90	0.533	2	
1714+5015	17 14 16.15	50 14 21.3	M25	19.40	5.43	0.9	2	
1714+5015	17 14 16.45	50 15 03.9	M126	19.14	2.86	0.275	3	
1714+5015	17 14 16.78	50 18 16.8	M49	13.89	3.29	0.0453	3	
1714+5015	17 14 16.91	50 17 36.7	M149	20.06	4.43	1.088	2	
1714+5015	17 14 17.07	50 18 06.7	M133	17.19	2.19	0.0457	3	
1714+5015	17 14 17.14	50 17 02.6	M167	18.91	3.95	1.361	2	
1714+5015	17 14 17.19	50 14 44.1	M39	20.47	2.18	0.362	3	
1714+5015	17 14 17.29	50 17 04.3	M169	19.62	2.51	0.53	3	
1714+5015	17 14 17.59	50 14 36.8	M35	19.33	4.00	1.278	2	
1714+5015	17 14 17.63	50 14 13.3	M22	19.90	3.65	0.73	3	
1714+5015	17 14 18.31	50 14 31.2	M33	20.04	2.19	0.291	3	
1714+5015	17 14 18.52	50 15 15.2	M120	20.11	4.47	0.825	2	
1714+5015	17 14 18.76	50 14 24.1	M26	18.74	5.62	0.749	2	
1714+5015	17 14 18.83	50 16 51.5	M174	18.35	3.83	0.276	3	
1714+5015	17 14 19.04	50 13 45.3	M6	18.78	3.54	0.653	1	
1714+5015	17 14 19.13	50 16 07.7	M86	18.11	3.64	0.995	2	
1714+5015	17 14 19.19	50 16 50.0	M170	20.57	4.75	3.391	1	
1714+5015	17 14 19.29	50 13 34.9	M3	19.98	3.70	2.217	2	
1714+5015	17 14 19.31	50 14 05.7	M18	19.42	3.31	0.77	3	
1714+5015	17 14 19.89	50 18 19.5	M57	20.05	3.14	0.046	3	
1714+5015	17 14 20.00	50 13 59.1	M16	19.80	2.94	0.568	3	
1714+5015	17 14 20.80	50 14 37.5	S31	19.46	2.99	0.596	3	
1714+5015	17 14 21.01	50 14 16.5	S21	18.31	4.55	0.751	3	
1714+5015	17 14 21.28	50 14 14.8	S20	18.92	3.56	0.804	3	
1714+5015	17 14 21.67	50 14 45.8	S35	18.52	5.70	1.206	2	
1714+5015	17 14 21.93	50 13 44.1	S7	19.15	5.30	2.548	1	
1714+5015	17 14 22.93	50 18 02.9	S64	18.63	6.35	1.236	1	
1714+5015	17 14 22.94	50 13 49.7	S10	19.13	3.22	0.759	3	
1714+5015	17 14 23.25	50 13 43.1	S5	19.33	4.67	0.753	2	
1714+5015	17 14 23.57	50 13 31.1	S0	17.70	4.72	0.707	2	
1714+5015	17 14 24.17	50 13 35.8	S3	19.46	2.70	0.269	3	
1714+5015	17 14 25.61	50 15 18.3	S52	19.55	3.41	0.751	3	
2359+068	00 01 29.92	07 12 12.1	N58	18.41	4.14	0.99	2	
2359+068	00 01 30.84	07 13 34.2	N55	19.03	3.05	0.425	3	
2359+068	00 01 31.34	07 13 45.2	N54	18.45	4.00	1.692	3	AGN
2359+068	00 01 32.49	07 12 03.6	N48	19.16	3.10	2.196	3	
2359+068	00 01 32.51	07 14 26.4	N49	19.53	2.46	0.397	2	
2359+068	00 01 33.62	07 14 31.6	N43	19.27	3.74	0.44	2	
2359+068	00 01 33.64	07 13 08.4	N42	19.30	4.49	0.801	2	
2359+068	00 01 33.96	07 13 31.5	N40	18.07	4.26	0.886	3	
2359+068	00 01 34.32	07 13 00.0	N37	18.33	2.44	0.621	3	
2359+068	00 01 34.33	07 12 48.2	N38	19.32	3.01	0.424	3	
2359+068	00 01 34.38	07 11 10.3	S72	18.18	2.75	0.582	3	
2359+068	00 01 34.92	07 14 23.6	N33	18.78	3.54	0.796	2	
2359+068	00 01 35.34	07 11 31.3	S71	18.18	4.01	0.829	3	
2359+068	00 01 36.74	07 13 05.9	N23	18.80	4.58	0.905	3	

TABLE 2—*Continued*

Field	R.A. (J2000.0)	Decl. (J2000.0)	Name	K Magnitude	$R-K$	Spectroscopic z	Quality[a]	Comments
2359+068	00 01 37.35	07 08 56.7	S57	19.31	5.06	2.204	1	
2359+068	00 01 37.69	07 14 09.7	N14	16.95	3.43	0.445	3	
2359+068	00 01 37.80	07 12 14.5	N13	19.06	3.04	0.355	3	
2359+068	00 01 38.09	07 09 58.3	S49	18.62	4.82	0.322	2	
2359+068	00 01 38.12	07 13 22.7	N12	18.15	3.95	0.885	2	
2359+068	00 01 38.17	07 13 53.5	N11	19.05	5.09	0.829	3	
2359+068	00 01 38.21	07 12 57.3	N10	18.34	4.20	0.66	2	
2359+068	00 01 39.60	07 11 10.7	S37	19.36	4.27	1.757	2	AGN
2359+068	00 01 40.00	07 14 05.3	N2	19.14	3.06	0.495	2	
2359+068	00 01 41.47	07 10 52.0	S26	19.59	3.24	0.444	2	
2359+068	00 01 41.65	07 09 58.2	S23	19.57	3.49	1.319	2	
2359+068	00 01 41.77	07 08 50.6	S21	19.00	3.19	0.415	2	
2359+068	00 01 42.59	07 10 37.0	S12	19.31	3.28	1.387	2	
2359+068	00 01 42.91	07 10 23.8	S10	20.55	3.67	0.177	3	
2359+068	00 01 43.07	07 09 01.2	S8	18.87	4.87	2.228	1	
2359+068	00 01 43.74	07 10 06.5	S4	19.24	>5.52	2.243	1	
2359+068	00 01 43.95	07 08 56.5	S3	20.32	2.31	0.917	3	
			Star Detections					
0149+336	01 52 13.35	33 51 44.0	S1	18.14	n/a	0		
0149+336	01 52 17.90	33 49 42.7	S49	19.93	3.107	0		
0149+336	01 52 18.94	33 51 10.9	S43	18.15	4.186	0		
0149+336	01 52 22.35	33 50 50.7	S24	19.23	4.275	0		
0149+336	01 52 31.25	33 49 26.9	S14	18.54	3	0		
0149+336	01 52 37.54	33 52 00.6	M13	20.23	3.873	0		
1107+7239	11 06 36.48	72 38 16.5	M30	17.56	4.354	0		
1107+7239	11 06 41.28	72 38 42.1	A41	18.48	3.469	0		
1107+7239	11 06 51.06	72 40 13.6	A30	18.51	3.29	0		
1107+7239	11 06 55.73	72 38 33.6	M15	16.56	3.465	0		
1107+7239	11 06 56.91	72 40 26.6	M14	19.69	3.43	0		
1714+5015	17 14 07.77	50 15 13.1	S53	19.85	4.504	0		
1714+5015	17 14 08.27	50 17 34.2	S76	18.93	5.668	0		
1714+5015	17 14 11.03	50 15 55.6	M90	19.91	3.584	0		Object 13[b]
1714+5015	17 14 13.12	50 17 39.2	M152	18.38	4.806	0		
1714+5015	17 14 13.43	50 13 54.1	M12	18.78	2.522	0		
1714+5015	17 14 14.26	50 17 40.4	M151	18.33	4.146	0		
1714+5015	17 14 15.10	50 15 20.0	M116	18.95	4.808	0		
1714+5015	17 14 15.16	50 17 17.2	M64	18.60	2.086	0		
1714+5015	17 14 16.77	50 13 52.9	M13	20.19	1.433	0		
1714+5015	17 14 23.63	50 17 20.6	S83	18.09	2.337	0		
1714+5015	17 14 24.58	50 14 27.2	S24	19.19	3.36	0		
2359+068	00 01 36.23	07 11 06.4	S67	19.62	2.329	0		
2359+068	00 01 40.10	07 09 39.2	S34	18.93	3.765	0		

NOTE.—Units of right ascension are hours, minutes, and seconds, and units of declination are degrees, arcminutes, and arcseconds. Table 2 is also available in machine-readable form in the electronic edition of the *Astrophysical Journal.*

[a] The quality of the spectroscopic redshift, where "3" is multiple emission lines (highest quality), "2" is a single emission line and absorption line or multiple absorption lines (medium quality), and "1" is a single emission line (lowest quality).

[b] Lyα emission-line objects from Pascarelle et al. (1996).

with redshift, making $J-K$ an excellent discriminant between stars and high-z galaxies (e.g., Drory et al. 2001). We exclude all $K<20$ sources from this region of color space from further analysis ($\sim$1.0 arcmin^{-2}), under the assumption they are cool dwarf stars. This cut is necessary as our photometric redshift code would often identify these red stars as early-type galaxies around $z\sim0.5$ or starbursts at $z>3$, confusing their cool colors with large 4000 Å or Lyman breaks. Altogether we removed 9% of the sources as contaminating stars, reducing the near-infrared sample to 764 sources. This contamination rate agrees with the roughly 10% star contamination rate at $K=19.5$–20 found in previous studies (Cowie et al. 1994; McLeod et al. 1995).

Of those identified, 18 redshifts come from single line identifications where the continuum was too weak to definitively corroborate the redshift. The lines are identified as Lyα from 3500 to 4500 Å and [O II] λ3727 from 6000 to 9300 Å. In 15 of these cases an optical through near-infrared photometric redshift agrees with the redshift derived from the single line, which demonstrates the galaxy does indeed have proper colors for its predicted redshift, making it unlikely the line has been misidentified. However, in three cases the photometric redshift disagreed with spectroscopic identification, once for Lyα (2359 S4) and twice for [O II] λ3727 (1107 M42 and 1714 M85).

2.2. *Targeted Redshift Overdensities Results by Field*

As discussed in Paper I, most of the fields included in this sample were targeted because of suspected overdensities at high redshifts. This included both known emission-line and absorption-line

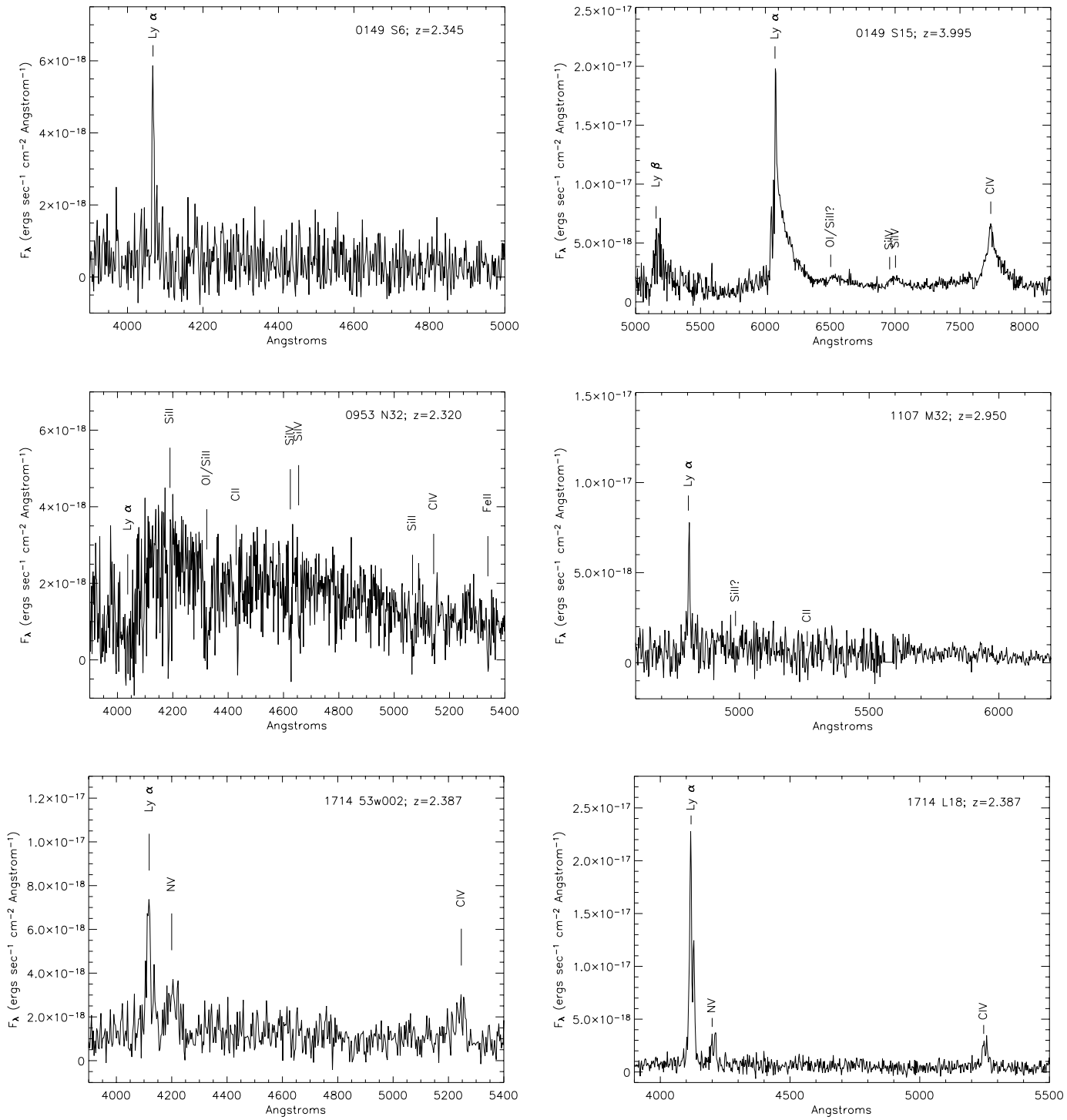

FIG. 1.—Spectra for 18 confirmed redshifts at $z > 1.5$. The identified broad-line AGNs are 0149 S15, 1714 L19, 1714 M36, and 1714 M129. The narrow-line AGNs are 1714 53w002, 1714 L18, 2359 N54, and 2359 S37.

objects, spanning the entire $z = 1$–2.5 Bright Ages and beyond ($z = 1.33$–2.87). Only the 1107+7239 field, included because of its deep WFPC2 data, contained no previously known high-redshift objects.

Of the five fields targeted for specific redshift overdensities, only one contained near-infrared–selected objects spectroscopically confirmed at that redshift, the 1714+5015 field (also known as the Hercules Deep Field). In addition to the three sources (53w002, L18, and L19) already known, we found only one further source, an AGN at a redshift of $z = 2.40$. We suspect that at the depths reached by our *K*-band survey, high-redshift sources with star formation vigorous enough to produce observable emission lines are rare. That is, to be included in this near-infrared survey with enough ultraviolet flux for redshift identification, galaxies need to be both reasonably massive and starbursting. Alternatively, the proposed high-redshift structures in most of our target fields are not real.

Two further possible overdensities have been identified in our survey, however. Four *K*-band–selected objects have spectroscopic redshifts around $z = 2.22$ in the 2359+068 field, while an another three are found around $z = 2.55$ in the 1714+5015 field. We also discovered two additional galaxies not detected in *K* band (i.e., blue

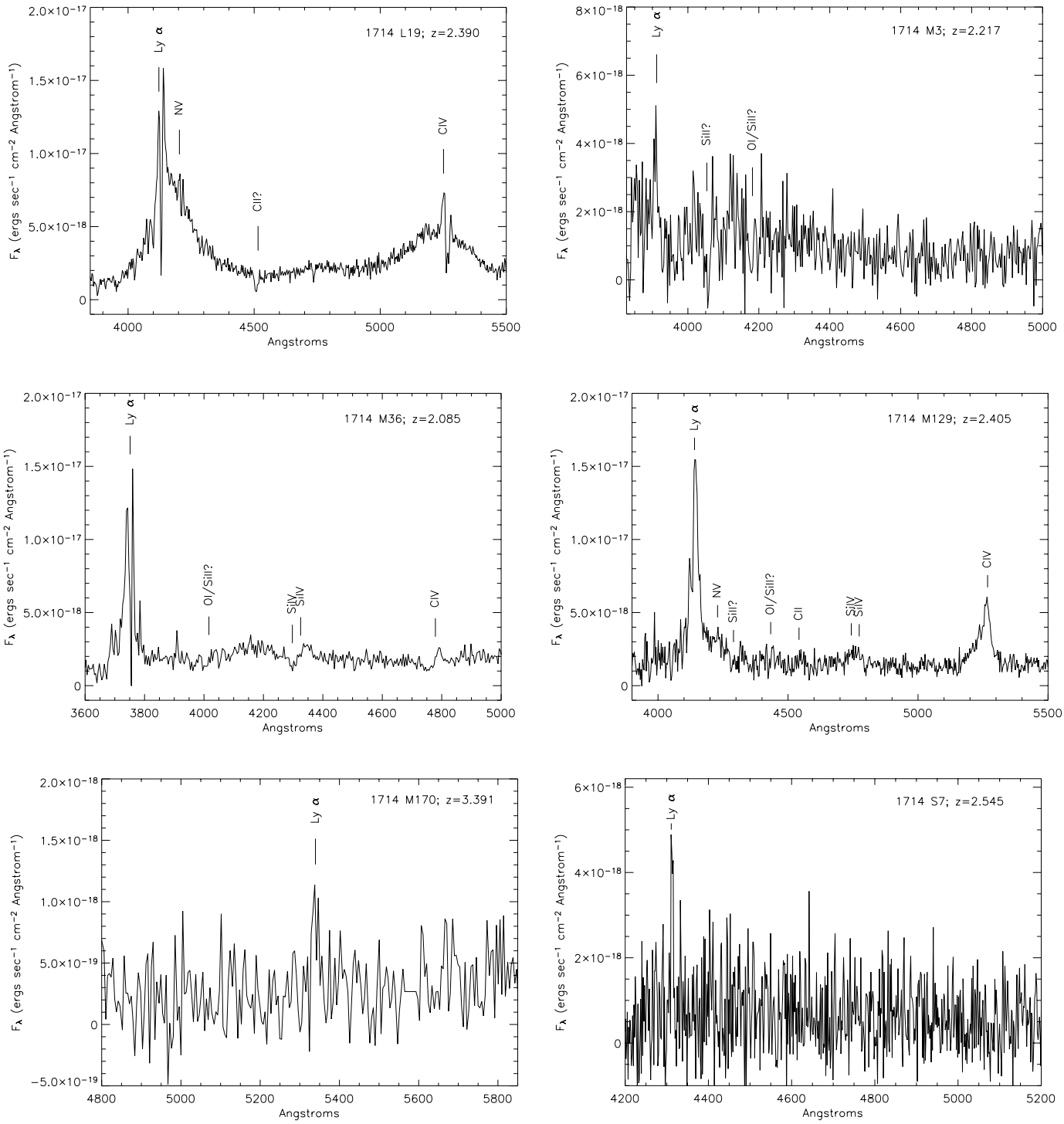

FIG. 1.—*Continued*

optically detected galaxies) at the possible $z = 2.55$ overdensity. In both cases of possible overdensity, the objects lie at $\pm$ 0.02 in z, which is roughly within the error for redshift identification of these sources, several of which were derived from a single, weak line.

3. PHOTOMETRIC REDSHIFTS

We produce photometric redshifts for all *K*-selected targets using both the photometric redshift program Hyperz version 1.1 (Bolzonella et al. 2000)[3] and the Bayesian photometric redshift code of Benitez (2000). Both codes produce redshifts by fitting a spectral energy distribution (SED) created from broadband photometry to a set of template spectra redshifted throughout the range of interest. Hyperz uses a χ^2 template fitting, while the Bayesian code uses a maximum likelihood method. The biggest difference between the two methods is that the Bayesian code weights the redshift estimates using a *prior* probability based on the redshift distribution and magnitudes of objects from the Hubble Deep Field–North. This reduces the number of high-redshift failures, as such galaxies are a priori much less common.

[3] See http://webast.ast.obs-mip.fr/hyperz.

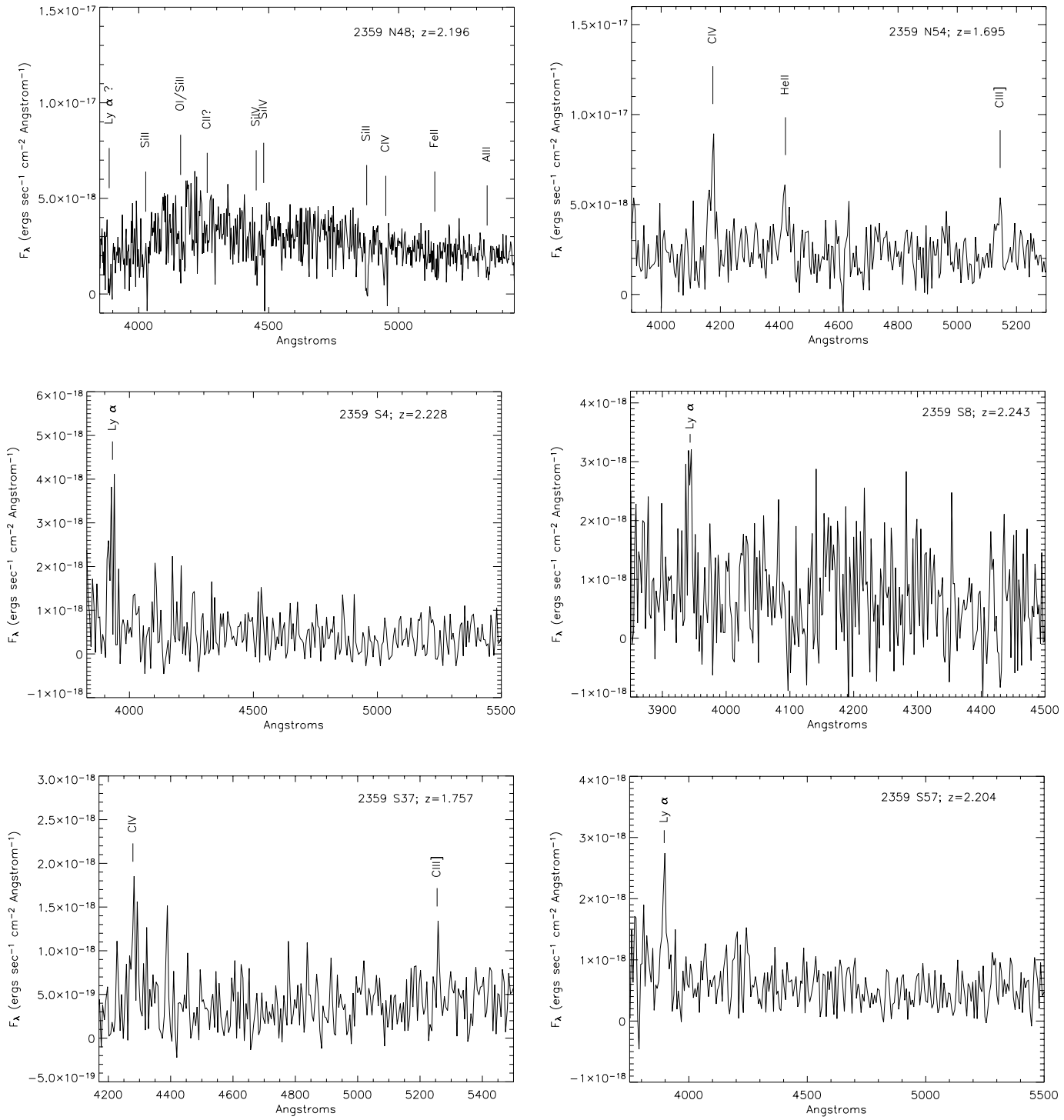

FIG. 1.—*Continued*

For Hyperz, we examined two sets of templates. The first was a simple set of mean spectra of local galaxies compiled by Coleman et al. (1980, hereafter CWW80) combined with two starburst templates of Kinney et al. (1996), which has been demonstrated to work well in the production of photometric redshifts (Fernandez-Soto et al. 2001). The second was a set of PEGASE.2 (Fioc & Rocca-Volmerange 1997) model templates including models that match local Hubble types (E, S0, Sa, Sc, and Im; Le Borgne & Rocca-Volmerange 2002) along with two burst models (250 and 500 Myr) and two continuous star formation models (4.5 and 2 Gyr). We tried a wide range of PEGASE models and found this nine-template set produced the best results for our data. Removal or replacement of one or two of the templates generally had only a small negative effect on the redshift accuracy, although one could not remove an entire class of template, such as all young starburst models or all old galaxy models. While a broad-line AGN template did produce a good fit to some of the known AGNs in our sample, we found that its inclusion produced too many redshift errors from star-forming galaxies being misidentified as AGNs. For dust extinction we apply the commonly used

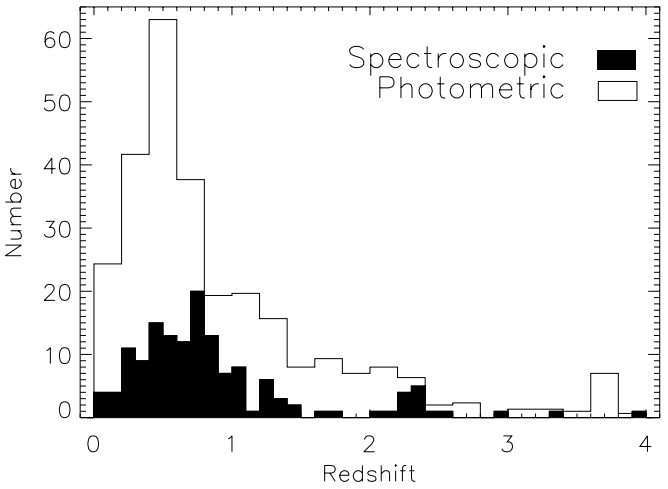

FIG. 2.—Filled histogram shows the distribution of all 146 redshifts with spectroscopic confirmations binned to 0.1 in z, excluding stars. On top is a histogram of all photometric redshifts binned to 0.2 in z, but then divided by 2 to maintain the visual relative difference in numbers to the spectroscopic redshifts. The photometric redshift sample includes the spectroscopic sample.

Calzetti et al. (2000) law, for ease of comparison with other work.

Hyperz also allows fits to an entire range of Bruzual & Charlot (1993) models, with different ages and exponential star formation rates. Despite better sampling all possible star formation histories, the Bruzual & Charlot model fits of the low-redshift galaxies are inferior to the simpler template fits. If we define a catastrophic photometric redshift failure as any photometric redshift different than its spectroscopic redshift by $\Delta z > 1$, then the full range of Bruzual & Charlot models produce twice as many catastrophic failures as the small sets of CWW80 or PEGASE templates: all low-redshift galaxies misidentified as high-redshift ones. As the Bayesian photometric code uses priors generated with the CWW80 + starburst set of models, we were only able to test that set of templates.

Two further steps were taken that had a strong impact on the quality of the photometric redshifts. The first is to limit the allowed redshifts to the range over which we expect to be able to detect even the brightest galaxies. For example, we predict only the relatively rare $(2–3)L_\star$ galaxies could be in our sample by $z \sim 3$. At $z > 4$ the required absolute magnitude becomes more than 2 mag above $L_\star$. We are therefore highly unlikely to miss any galaxies by making $z = 4$ the highest allowed redshift, while removing a large template fitting space that only leads to bad photometric redshifts. This step alone reduces the number of catastrophic failures by more than 40%. The second step is to add an estimate for the systematic errors contained in all the photometry data, which were taken at different times, under different weather conditions, and at several different telescope sites. This systematic error could then be added (in quadrature) to the photometric errors obtained from SExtractor. We applied a systematic error of both 5% and 10%. While the 10% error makes the fit of photometric to spectroscopic redshifts slightly worse, a 5% systematic error reduces catastrophic failures by 15% and reduces dispersion of the photometric redshifts by 10%. Indirectly, as a sort of consistency check for the entire system of photometry, this shows that the calibrations and photometry extractions are generally sound, at least to within ~5%.

Both photometric redshift codes produce very similar results using the same CWW80 + starburst templates. Comparison to

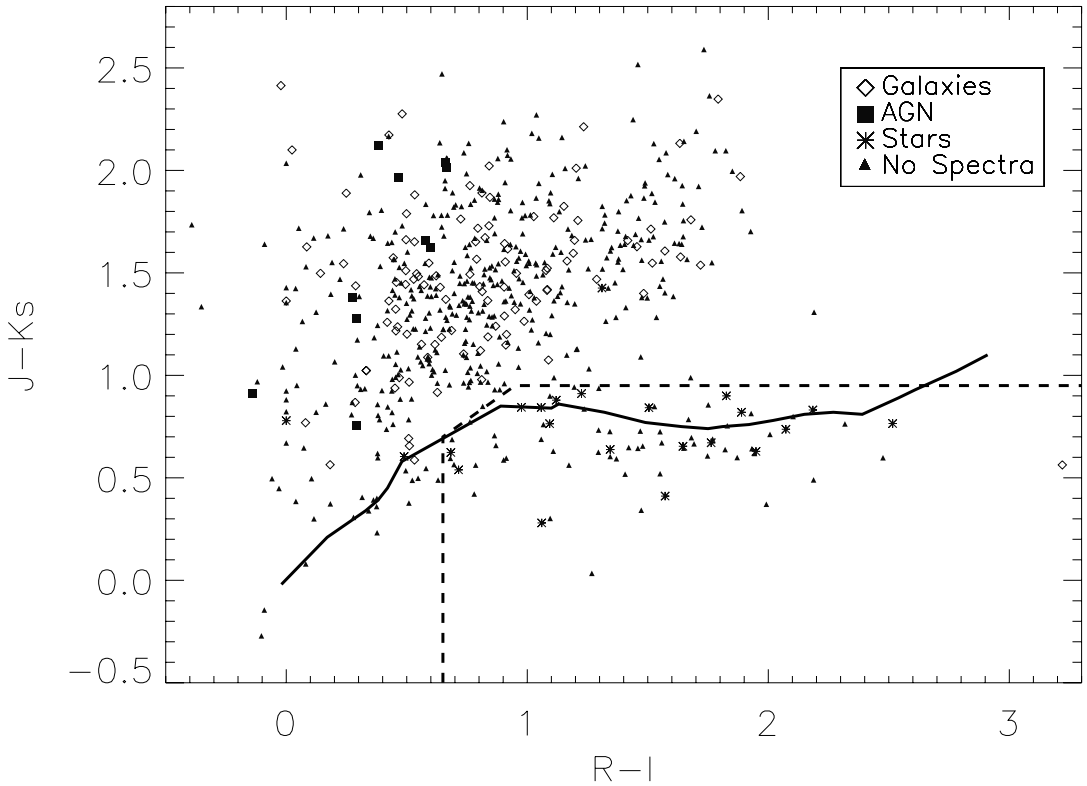

FIG. 3.—Color-color diagram of $R - I$ vs. $J - K$ for all sources with $K < 20$. Galaxies are marked by empty diamonds, AGNs by filled squares, stars by asterisks, and objects without spectroscopic identification by small filled triangles. The dotted line marks the region populated almost exclusively by stars that we have excluded form the final sample. The solid line is a stellar track extending to 2000 K (the coolest stars in our sample are 2400 K). The track is from the NMARCS M dwarf models of Bessell et al. (1998).

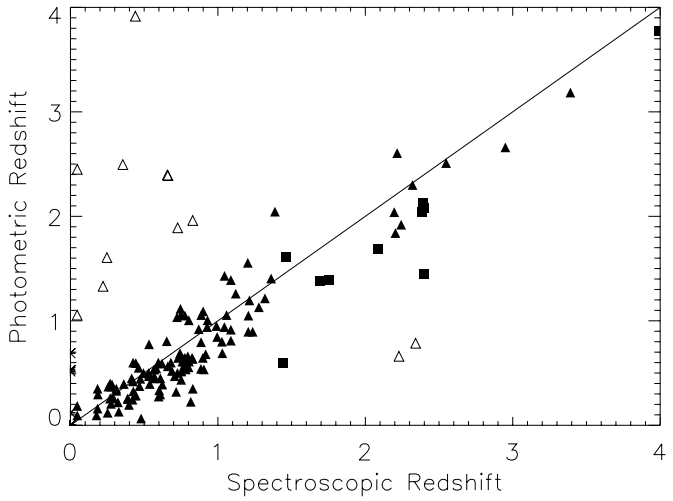

FIG. 4.—Plot of photometric redshifts vs. spectroscopic redshift for all K-band–detected objects. Galaxies are marked with triangles, while AGNs are marked with squares. Catastrophic errors are plotted as open symbols. Stars remaining (four) after the $J - K$ vs. $R - I$ color cut are plotted with an asterisk at a spectroscopic redshift of 0.

the spectroscopic redshifts (see below) produces almost identical $\sigma_z/(1 + z)$ and numbers of catastrophic failures. However, the PEGASE model templates, which cover a slightly broader range of possible star formation histories, produced a $\sigma_z/(1 + z)$ 35% lower with no increase in catastrophic failures, making it clearly superior for analysis of this data set. As the Bayesian photometric code could not easily incorporate the PEGASE models and no significant difference was seen for the CWW80 + starburst templates, we chose to use the Hyperz redshifts found from fitting PEGASE templates for all further analysis.

Figure 4 presents the results of our use of photometric redshifts by comparing them to the spectroscopic redshifts found using LRIS. Out of 148 spectroscopic redshifts obtained for infrared-detected objects, only 12 are catastrophic failures, a rate of ~8%. At redshifts below $z = 1.5$ the contamination from catastrophic photometric redshifts is not significant and can be disregarded for further analysis. However, at $z = 1.5$–2.5 the low-redshift catastrophic failures make up a significant percentage of the galaxies within that redshift range (~33%). We apply a correction for this contamination before any final analysis (see § 4 below).

The dispersion of photometric redshifts to the spectroscopic redshifts, σ_z, equals 0.23 if the catastrophic failures are not included. A better statistic is $\sigma_z/(1 + z)$, which takes into account that what we are interested in is not absolute redshift accuracy, but accuracy relative to each redshift. For our sample we measure $\sigma_z/(1 + z) = 0.11$. This dispersion is roughly 50% greater than some of the published photometric redshifts with spectroscopic confirmations (e.g., Fernandez-Soto et al. 2001; Rudnick et al. 2001; Chen et al. 2003), although it is superior to the dispersion required to include all photometric redshifts from the blind test of Cohen et al. (2000).

Most photometric redshift studies to date have shown what photometric redshifts can do with the best of data, while this study is more of a realistic "road test," demonstrating how well photometric redshifts can operate even when all conditions are not optimal. The photometric redshifts from this study were produced using many different sources, with large differences in depth, seeing, and calibration reliability. Only 12 of the 76 arcmin^2 have complimentary optical *Hubble Space Telescope* (*HST*) WFPC2 data, while the rest of the optical data is a mixture of Keck LRIS and Lick PFCam. Even with these complications, our photometric redshifts are reliable to ~10% in $(1 + z)$, with a manageable amount of catastrophic errors. Statistically, almost as many high-redshift galaxies are missed as included and both are smaller numbers than the amount of galaxies at the correct predicted redshift. This allows studies of large ranges of redshift space, where a 10% error will have little effect.

4. GALAXIES IN THE BRIGHT AGES

In all, this project spectroscopically confirms 39 infrared-detected objects with $z > 1$, thirty-five of which fall into the key $z = 1$–2.5 region, which we refer to as the Bright Ages, because it may be the epoch in time in which the bulk of star formation and galaxy assembly took place. For further analysis we divide the Bright Ages into two redshift ranges, $z = 1$–1.5 and $z = 1.5$–2.5, and also include a lower $z = 0.5$–1.0 range to examine evolution.

We focus on the less-studied $z = 1.5$–2.5 redshift range, over which the entire near-infrared data set produced 103 photometric redshifts with 14 spectroscopic confirmations. Comparison to the spectroscopic data found more (seven) falsely included objects than those improperly identified as low redshift (two), suggesting contamination could be as high as ~25%. This is almost certainly an overestimate of the contamination rate, as there is a strong bias against confirmation of high-redshift sources, because of their low flux and lack of strong features, particularly from $z = 1.5$–2. Only about half of the high-redshift photometric candidates observed produced a redshift, so the contamination rate seen in the spectroscopic sample may be half that of the full photometric redshift sample. A more careful analysis examining the absolute magnitudes of the failed photometric redshifts finds that only the brightest end of the luminosity function ($-24.5 > R > -25.0$) is significantly contaminated, with contamination at lower luminosities $\leq$5%.

There are only a small number of $z = 1.5$–2.5 galaxies with spectroscopic redshifts estimated to be brighter than $-24.0:1$ correctly identified and three bad high-z photometric redshifts. These few galaxies suggest a contamination rate of 38%–75%, depending on how many of the $z = 1.5$–2.5 candidates that produced no spectroscopic redshifts are actually within the predicted redshift range. For the sake of simplicity we assume a contamination rate of 50% for the $-25.0 > R > -24.5$ bin, noting that the exact choice makes very little difference to the final statistics. All subsequent analysis uses this contamination correction.

Of all the confirmed, near-infrared–selected $z > 1.5$ galaxies, eight are AGNs. The AGN fraction of 8 out of 18 or 44% appears on the surface to be high. We recall, however, that three of these are previously known AGNs from the 1714+5015 field; this field's high density of AGNs and high-redshift structures (see Keel et al. 1999) were key factors in our selecting the 1714+5015 field for this survey. Removing those three AGNs gives a rate of 5/15, or a 33% contamination for studying the normal star forming galaxies of the universe. However, this rate must also be considered to be somewhat of an upper limit, as the redshifts of AGNs are more likely to be confirmed because of their numerous strong emission lines. As only half of the observations of near-infrared sources produced spectroscopic identifications, the true AGN contamination rate is likely closer to 15%–20%. Further, only half (4) of these AGNs have broad lines. The total ultraviolet/optical light output of narrow-line AGNs are often dominated by their star formation (i.e., Malkan et al. 1996; González Delgado et al. 1998), so they should not automatically be considered a contaminant in a star-forming galaxy sample.

Only the known broad-line AGNs are excluded in the following number counts, estimates of dust extinction and star formation.

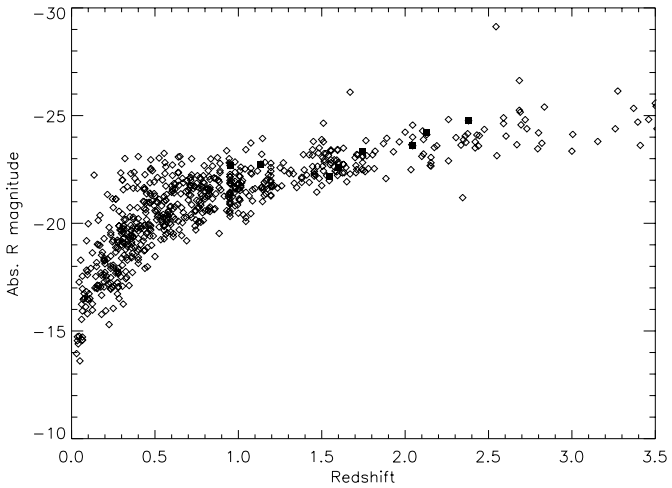

FIG. 5.—Distribution of all photometric redshifts vs. their predicted absolute R magnitude over 76 arcmin^2. Known AGNs are marked with filled squares.

We do no attempt to statistically remove undiscovered broad-line AGNs from the full photometric redshift sample, as it is unclear whether they should be removed equally from all luminosities or only from the highest luminosity bins. The broad-line AGNs likely represent a contamination rate well below their ~20% representation in the spectroscopically confirmed $z > 1.5$ sample and should therefore have only a minor effect on the final analysis.

Figure 5 plots the derived absolute R magnitude against photometric redshift for our sample. The graph shows a smooth trend of decreasing counts and slowly increasing maximum magnitude with redshift. Another check that the photometric redshift code is behaving well is a general lack of extremely bright galaxies, with only three greater than $M_R = -25$ out to $z = 2.5$, despite having the freedom to produce galaxies up to $M_R = -28$ (only one has been plotted). The three anomalously bright galaxies are assumed to be low redshifts misidentified as high redshift and are not included in any of the following analysis. Figure 6 shows a distribution of best-fit model templates for different redshift bins, demonstrating that the entire range of templates were used to fit the input SEDs. Lower redshift galaxies ($z = 0.5$–1) have a much larger percentage of galaxies fit by templates matched to typical local SEDs, i.e., elliptical (E) through irregular (Im). As the redshift increases the percentage of galaxies fit by the younger templates, 4.5 Gyr continuous star formation (Im2) through 250 Myr

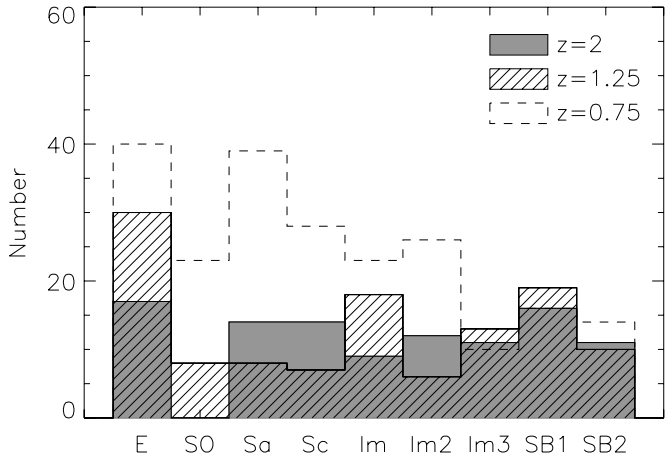

FIG. 6.—Distribution of best-fit model templates from Hyperz for $z = 0.5$–1 (*dashed histogram*), $z = 1$–1.5 (*hatched histogram*), and $z = 1.5$–2.5 (*solid histogram*) redshift bins.

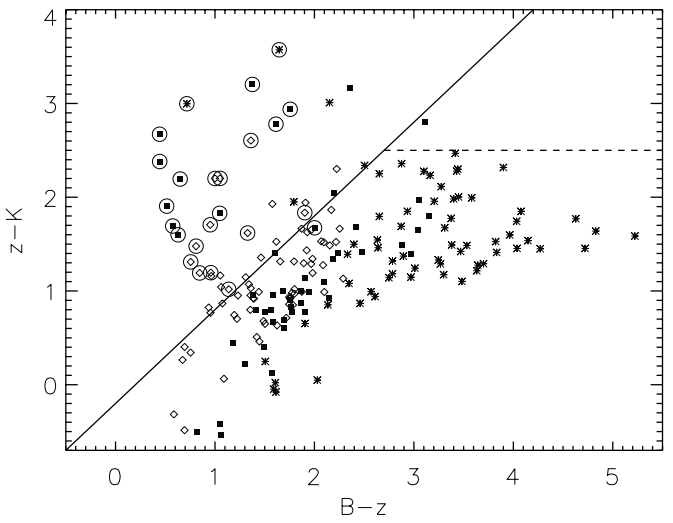

FIG. 7.—*BzK* diagram ($B - z$ vs. $z - K$) for the 1714+5015 field. The solid and dashed lines mark the *BzK* dividing lines for star-forming and old $z > 1.4$ galaxies, respectively. Asterisks represent galaxies fit by older templates (E, S0, Sa), filled squares represent intermediate age template fits (Sc, Im), and the diamonds represent young galaxy template fits (Im2, Im3, SB1, SB2). Galaxies with photometric redshifts of $z > 1.4$ are circled.

starbursts (SB2), also increases, although there is little statistical significance between the $z = 1$–1.5 and $z = 1.5$–2.5 distributions.

4.1. *Comparison to Other Bright Age Selection Methods*

We can compare our K-selected, photometric redshift sample to other $z = 1$–2.5 selection methods. The *BzK* selection method (Daddi et al. 2004) identifies $1.4 < z < 2.5$ galaxies in K-selected samples from their $z - K$ and $B - z$ colors. Only one of our fields, 1714+5015, has the necessary matching deep z'- and B-band data to produce a *BzK*, which we present in Figure 7. The *BzK* method does a good job differentiating young from intermediate from old galaxy templates. In general, we find our $z > 1.4$ photometric redshifts in strong agreement with the *BzK* selection criteria, with the possible exception of the reddest ($B - z$) galaxies. We find a similar density of $z > 1.4$ objects down to $K = 20$, ~1 arcmin^{-2}. We also find that the redder $z - K$ objects that Daddi et al. (2004) identify as star-forming are being fit by intermediate to old models, which is probably a reflection of the strong 4000 Å break required to produce such a strong $z - K$ color. This does not necessarily imply a lack of significant star formation in these galaxies; rather the template fitting may be more sensitive to the strong spectral break. $J - K$ versus $R - K$ (or $I - K$) color-color diagrams have also been suggested as a tool for separating star-forming from elliptical ERO galaxies (Pozzetti & Mannucci 2000; Cimatti et al. 2003), with the reddest galaxies fit by the older templates. Our best-fit templates for EROs ($R - K > 5.3$) do not show such a clear old versus star-forming separation, with many old template fit galaxies appearing on the star-forming part of the diagram.

Extremely red near-infrared color ($J - K > 2.3$) can also be used to identify red galaxies at $z > 2$ (Franx et al. 2003; van Dokkum et al. 2003), often referred to as distant red galaxies (DRGs). Our sample is not well suited for identifying these objects, as the color difference of the majority of the J and K limits is only $J - K \approx 1.2$, requiring K magnitudes 2 mag brighter than the typical K-limit of DRG surveys ($K \sim 21$). However, we do find eight $J - K > 2.3$ DRGs in our survey, four of which have photometric redshifts of $z > 1.5$ (one young template, three old). This hints that our photometric redshift selection may be

missing some of the oldest $z \sim 2$ galaxies. Similarly, the *BzK* sample of Reddy et al. (2005) failed to select almost a third of their DRG sample. We should, however, be cautious drawing too many conclusions from such a small number of galaxies.

Large numbers of $z \sim 2$ galaxies are also being found in rest-wavelength ultraviolet samples, such as the $1.5 < z < 2.5$ BX/BM objects, which are found by extending the Lyman break detection technique to lower and lower redshift (Adelberger et al. 2004; Steidel et al. 2004). Only three of our fields have the necessary *UBR* data to allow a similar analysis after converting to the $\mathcal{U}_n G\mathcal{R}$ system (Steidel & Hamilton 1993). Every object with the BX/BM color selection criteria is also identified as high redshift by our photometric redshifts. However, even accounting for errors in filter conversion and photometry, we estimate that the BX/BM method could select at most two-thirds of our $z > 1.5$ photometric redshift sample. This is comparable to the 60% recovery rate of $K < 20$ *BzK*-selected sources Reddy et al. (2005) found for their BX/BM galaxies, but much higher than the 5%–12% recovery rate found for DRGs.

4.2. *R Magnitude Luminosity Functions*

We produce luminosity functions for the three different redshift bins: $z = 0.5$–1, $z = 1$–1.5, and $z = 1.5$–2.5. Since our number statistics are falling rapidly as we approach $z = 3$, we leave an examination of any higher redshift out of our analysis.

To create luminosity functions, we have to take into account that in a flux-limited sample not every galaxy is sampling the entire volume of the redshift bins. If a galaxy at the detection limit is found at the closer edge of the redshift bin, it is only probing a small volume. To address this we use the method of $V_{\max}$ (Felten 1977), where every galaxy has a maximum volume within which a galaxy of that absolute magnitude could still be detected, depending on the flux limit of the field. The value $1/V_{\max}$ is then the number density if there was just that one galaxy in the field. One can then add up all the densities to find the true one, with only a final adjustment for the actual solid angle of the sky observed, as given below:

$$\delta_{\rm gal} = \frac{4\pi}{\Omega} \sum 1/V_{\max} \qquad (1)$$

The only remaining issue is dealing with fields that reach differing flux limits. While the $V_{\max}$ method accounts for lower counts from shallow fields by dividing by a smaller volume, it cannot account for a situation where zero counts are added as then there is no measurement of the volume that has been sampled by the field. For example, one could imagine covering two fields, one small and deep, the other wide and shallow. If no galaxies are detected in the wide field, then multiplying by $4\pi/\Omega$ would greatly decrease the number density, even if the wide field sampled virtually no volume at all. To account for this issue we find the luminosity function for each field and then average the final bins together, weighted by the volume each bin could sample for each field. Both the $V_{\max}$ calculated for each galaxy and the $V_{\max}$ calculated to determine weighting for each bin require small *K*-corrections to determine what the apparent *K* magnitude would be at increasing redshift. For this we employ the model templates and dust extinction used to fit the photometric redshift in the first place. For the average bins we used the model appropriate for a young stellar population. Because volumes beyond their redshift bin did not need to be probed, these *K*-corrections were never large. Completeness corrections are applied for galaxies at the faintest end of the distribution, although these are never more than 20%, i.e., we did not use galaxies detected below the 80% completeness level.

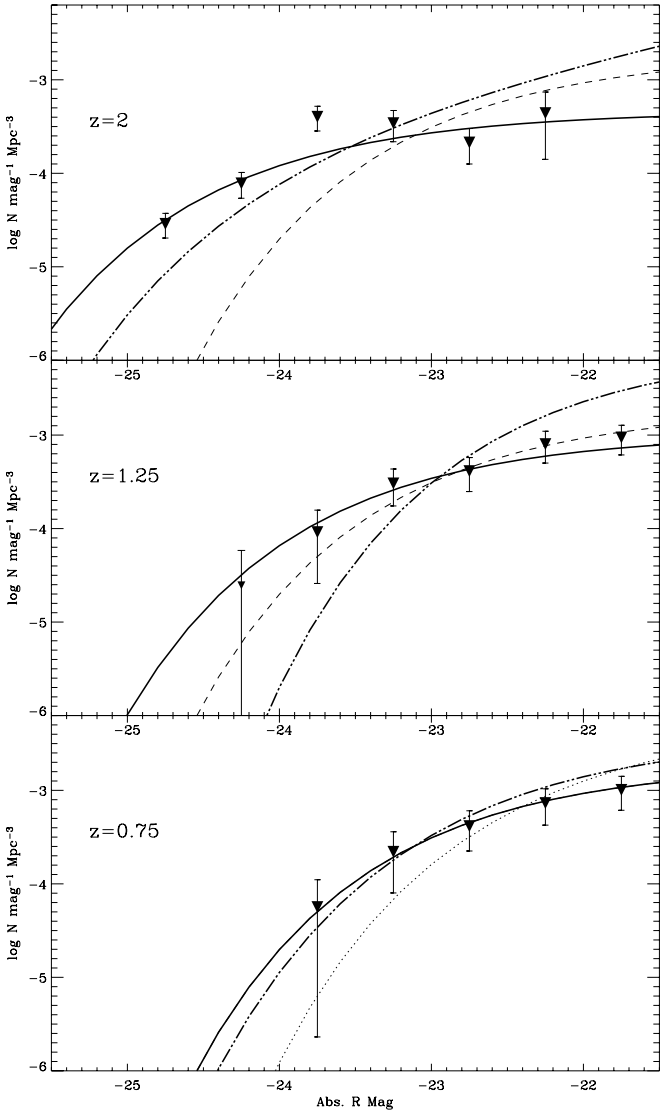

FIG. 8.—Rest-wavelength *R*-band luminosity functions for all *K*-selected galaxies. The solid lines are the fits to the data, with α set to -1.0. The dashed lines are the $z = 0.5$–1.0 Schechter fits plotted at $z = 1.25$ and $z = 2$ for reference. The double-dot–dashed lines show comparison *R*-band Schechter fits from the literature: we compare the LCIRS for $z = 0.5$–1.0 and $z = 1.0$–1.5 (Chen et al. 2003), while for $z = 1.5$–2.5 we compare to the $z = 3$ rest-wavelength *V*-band counts taken from Shapley et al. (2001) and corrected by $V - R = 0.5$. The local *R*-band luminosity function (Blanton et al. 2001) is also plotted as a dotted line in the bottom plot for comparison.

Figure 8 shows the final *R* absolute magnitude luminosity functions. We overplot the best-fit Schechter luminosity functions for each redshift bin with the low-luminosity slope, α, fixed at -1.0. We chose a fixed value of α because generally we do not measure enough faint galaxies to robustly determine it, particularly at the higher redshifts. By keeping α constant we can more reliably compare luminosity functions across different redshifts and even against different studies, such as the Las Campanas Infrared Survey (LCIRS; Chen et al. 2003), which also used a fixed $\alpha = -1.0$. Our final fitted Schechter values of ϕ_* and M_{R*} are given in Table 3. The errors bars for all points include an estimate for the effects of cosmological variance as described in Somerville et al. (2004).

We also plot the *R*-band fits from the LCIRS for the $z = 0.5$–1.0 and the $z = 1.0$–1.5 redshift bins. Chen et al. (2003)

TABLE 3
Results of Schechter Function Fits

	All Galaxies ($\alpha = -1.0$)			E/S0/Sa ($\alpha = -0.2$)		
Redshift Range	ϕ_* (10^{-3} Mpc^{-3})	M_{R*}	No. of Galaxies	ϕ_* (10^{-3} Mpc^{-3})	M_{R*}	No. of Galaxies
$z = 0.5$–1.0	2.08 ± 0.71	-22.35 ± 0.30	228	1.25 ± 0.38	-22.03 ± 0.33	102
$z = 1.0$–1.5	1.12 ± 0.33	-22.90 ± 0.30	119	1.17 ± 0.46	-21.63 ± 0.32	46
$z = 1.5$–2.5	0.50 ± 0.15	-23.68 ± 0.22	103	0.34 ± 0.16	-22.71 ± 0.29	31

produced separate Schechter fits for bins of $z = 0.5$–0.75 and $z = 0.75$–1.0, so what is plotted is actually an average of the two luminosity functions. There is general agreement at the lower redshifts ($z = 0.5$–1.0), but the LCIRS $z = 1.0$–1.5 fit has a substantially larger ϕ_*. However, the LCIRS $z = 1.0$–1.5 luminosity function is fit to only two points, so it may be too shallow ($H < 20$) to robustly measure the luminosity function above $z > 1$. For comparison we also plot the local R-band luminosity function from Blanton et al. (2001), derived from over 11,000 galaxies in the Sloan Digital Sky Survey (York et al. 2000). The Blanton et al. (2001) luminosity function produces a substantially higher luminosity density than earlier studies (i.e., Lin et al. 1996; Folkes et al. 1999).

For the highest redshift bin we compare to $z = 3$ points from the infrared study of Shapley et al. (2001). At $z = 3$, the K filter samples rest-frame V, not R, so a correction of $V - R = 0.5$, appropriate for a galaxy dominated by a young stellar population, has been added to the Shapley et al. (2001) V absolute magnitudes. A bluer correction shifts the line right, while a red correction would move it left. The color correction would have to be systematically wrong by at least 0.5 mag to substantively change the results. While not optimal for comparing to an infrared-selected sample, Lyman break galaxies represent the bulk of what we currently know about the $z > 3$ universe.

The R-band luminosity functions show a clear increase in the brightness of M_{R*} with redshift, combined with what appears to be a gradual reduction in ϕ_*. This would suggest a combination of both luminosity and number evolution, although the ϕ_* evolution is more uncertain, relying more heavily on the measurement of the faintest points for which the measured change between redshifts is typically less than their error bars. We must be cautious comparing to the Shapley et al. (2001) $z = 3$ points, as they were selected in a very different manner, but they would indicate a reversal of this trend at higher redshifts.

One possible explanation for the large number of $z = 2$ bright galaxies is that the photometric redshift contamination rate is higher than estimated, leading to an artificial inflation in the number counts. Another alternative explanation is that the $z = 3$ data is missing counts, possibly because of strong dust extinction, removing them from their rest-wavelength ultraviolet-selected sample. The final possibility is that the plot is correct and that the M_{R*} does indeed reach a peak around $z = 2$, before falling to $z = 3$. This would mean that $z = 1.5$–2.5 redshift range is indeed the Bright Ages, the epoch when the greatest number of the brightest galaxies existed.

Similar trends can be seen in the data sets of some of the other groups working with deep infrared photometric redshifts. Kashikawa et al. (2003) examine the $2' \times 2'$ Subaru Deep Field, also using the Hyperz software. Although they report B-band luminosity functions, they also find an increase in the fraction of the most luminous galaxies to $z = 2$, followed by a decline at even higher redshifts. Pozzetti et al. (2003), using the K20 sample of galaxies, also notes this increase in the number of bright galaxies in their luminosity functions, although they use rest frame J- and K-band magnitudes requiring large extrapolations from their observed near-infrared photometry for the highest redshifts examined by their analysis ($z \sim 1.5$).

We also examine the luminosity function evolution of the more evolved galaxy population separately. Figure 9 shows the R-band luminosity functions for all galaxies fit by E, S0, or Sa

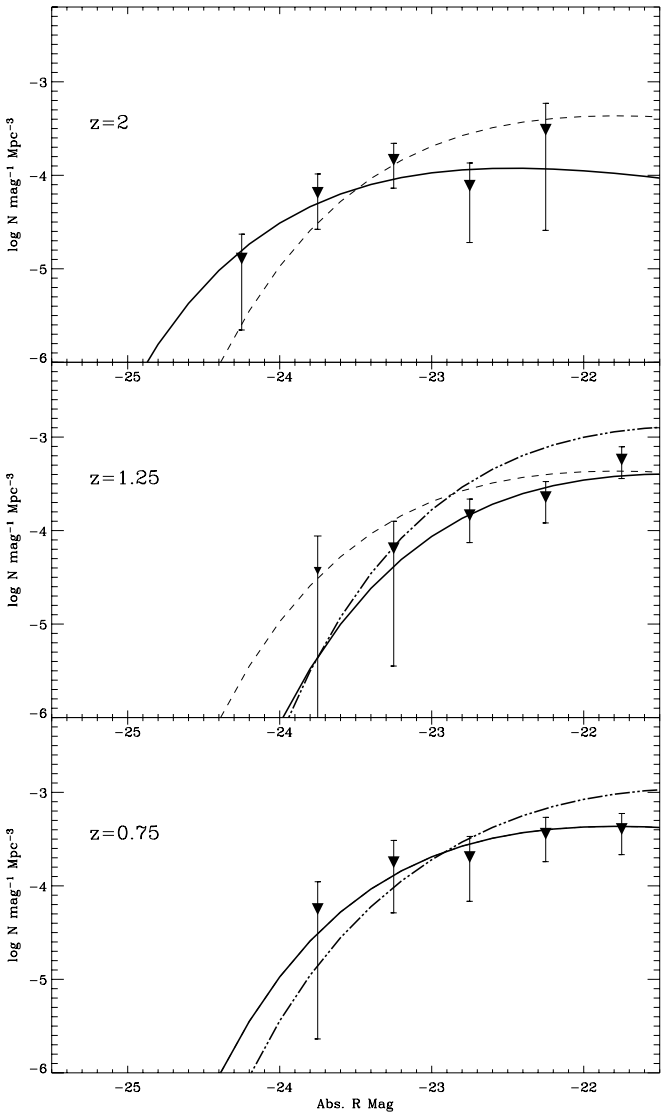

Fig. 9.—Rest-wavelength R-band luminosity functions for K-selected galaxies fit by E, S0, or Sa templates. The solid lines are the fits to the data, with α set to -0.2. The double-dot–dashed lines are R-band Schechter fits to similarly old/red templates from Chen et al. (2003). The dashed lines are the $z = 0$–1.0 Schechter fits plotted at $z = 1.25$ and $z = 2$, for reference.

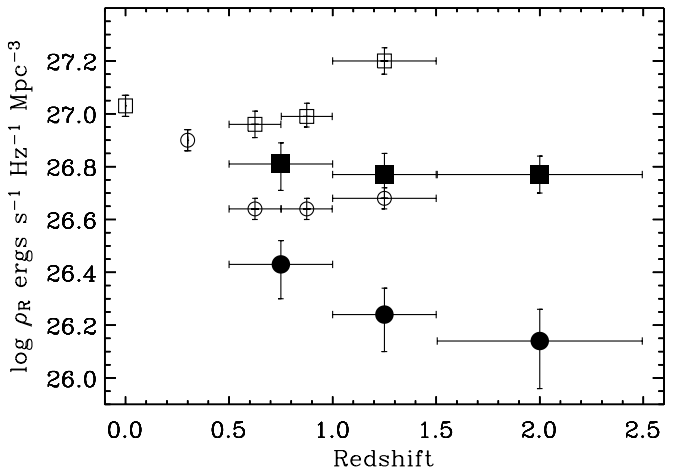

FIG. 10.—*R*-band luminosity density as a function of redshift. Densities including all galaxies are plotted as squares, while densities for old template fits are plotted as circles. Data from this study are solid points, while data from the literature are hollow points. These data include Blanton et al. (2001) for $z = 0.0$, Lin et al. (1999) for α, and Chen et al. (2003) for the points at $z = 0.5$–1.5.

templates at each redshift bin. The slope of faint galaxy counts is clearly falling, so we choose a fixed $\alpha = -0.2$, matching the α used by Chen et al. (2003) for their sample of evolved galaxies (E/S0 or Sab). There is no significant evidence for evolution between $z = 0.5$–1.5, with both the changes in luminosity density at each magnitude and the fitted Schechter parameters being less the measured errors. The drop in number density and increase in M_{R*} out to $z = 2$ appears more significant. It should be cautioned, however, that the faint luminosity end is highly uncertain because of the decreasing number of available galaxies at these high redshifts. Comparison to the Chen et al. (2003) evolved galaxy luminosity functions consistently shows fewer faint galaxies, but this could simply be a result of using different template fits. The general trend, little change from $z = 0.5$ to $z = 1.5$, is the same.

By integrating the derived luminosity functions we can follow the evolution of the total *R*-band luminosity density, ρ_R, with redshift, which we present in Figure 10. The ρ_R of the complete *K*-selected sample stays approximately constant over the entire examined redshift range, $z = 0.5$–2.5, with the increases in M_{R*} roughly canceled by decreases in ϕ_*. We can contrast the total sample result with the evolution of the ρ_R of evolved galaxies, which drops steadily out to $z = 2.5$. This trend indicates that more evolved galaxies are becoming a larger percentage of the total *R*-band luminosity with decreasing redshift. The Chen et al. (2003) results would appear to disagree with both trends, showing a rise in ρ_R with redshift for all galaxies and no change in ρ_R for evolved galaxies. However, as noted before, the $z = 1$–1.5 results are relatively shallow and fit to a small number of bright galaxy luminosity bins, and should therefore be treated with caution. Even so, the Chen et al. (2003) data still shows an increase in the *ratio* of evolved galaxy to total galaxy ρ_R from $z = 1.5$ to $z = 0.5$. Not much should be made of the absolute differences between the evolved galaxy ρ_R of our study and that of Chen et al. (2003), as they were derived using different templates. The $\sim$0.2 dex difference for total galaxy ρ_R is comes mainly from a higher ϕ_* for the Chen et al. (2003) luminosity function, demonstrating how small differences in fits can lead to larger ($\sim$50%) differences in the integrated ρ_R value.

Because we targeted regions of suspected overdensity, there is a possibility that the derived luminosity functions and densities measured in redshift bins that overlap these possible redshift density peaks might be elevated from what one would find in a random pointing. To address this issue, we also examined the redshift range from $z = 1$ to $z = 2$, which lies well away from the redshifts of the majority of the overdensities (i.e., $z = 2.16$, 2.39, 2.50, 2.83, 2.87). In general all the $z = 1$–2 results fall smoothly between those measured at $z = 1$–1.5 and $z = 1.5$–2.5, except for the measured counts in the range $-24 < R < -23.5$. The $z = 1$–2 luminosity function does not show the large rise in counts at that magnitude that can been seen in the $z = 1.5$–2.5 counts. This could be an artifact of the photometric redshift method, with a substantial population of galaxies misidentified at $z = 2$–2.5. However, no significant contamination was seen in the spectroscopically confirmed sample at these magnitudes. The significant contamination was for the brightest bins ($-25 < R < -24$). Alternatively, this could be a signal of the suspected overdensities, particularly if the luminosity function of these overdense regions

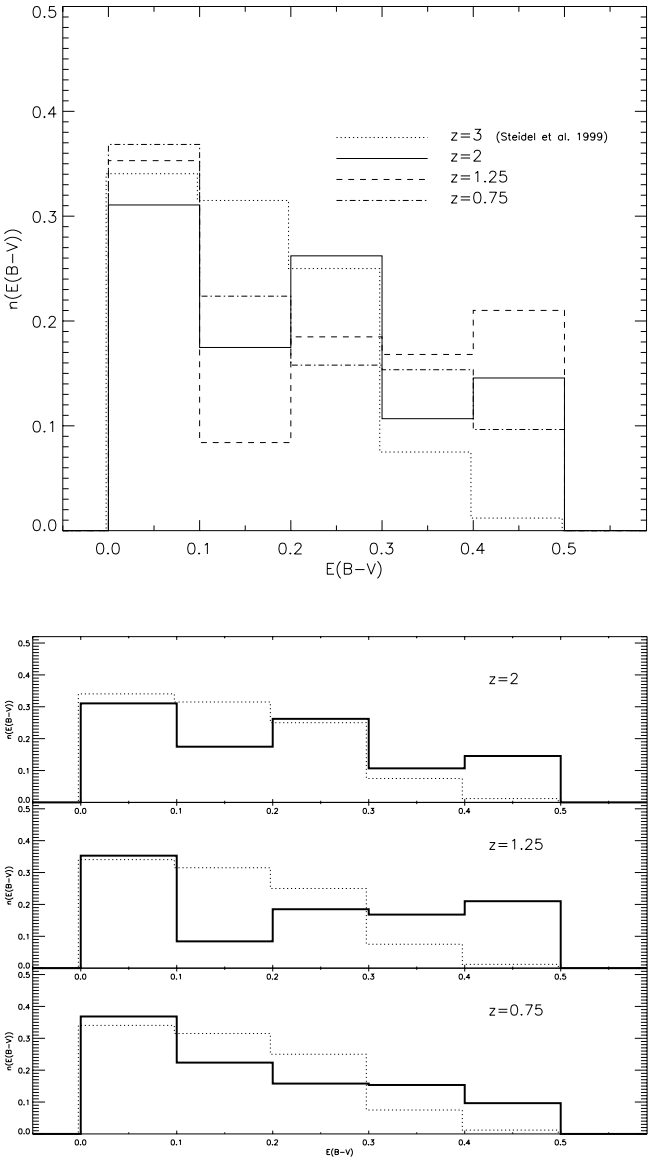

FIG. 11.—*Top:* The normalized distribution of $E(B - V)$ derived from photometric redshift fits and a Calzetti et al. (2000) dust extinction law are plotted for different redshifts. The solid line is our $z = 1.5$–2.5 data, the dashed line is $z = 1$–1.5, and the dot-dashed line is $z = 0.5$–1. The Steidel et al. (1999) data for their $z \sim 3$ Lyman break galaxies is the dotted line. All negative $E(B - V)$ values from their original plot have been placed into the lowest $E(B - V)$ bin. *Bottom:* Same graph, but with each redshift histogram plotted separately using a solid line. The Steidel et al. (1999) data is plotted each time as a dotted line for comparison.

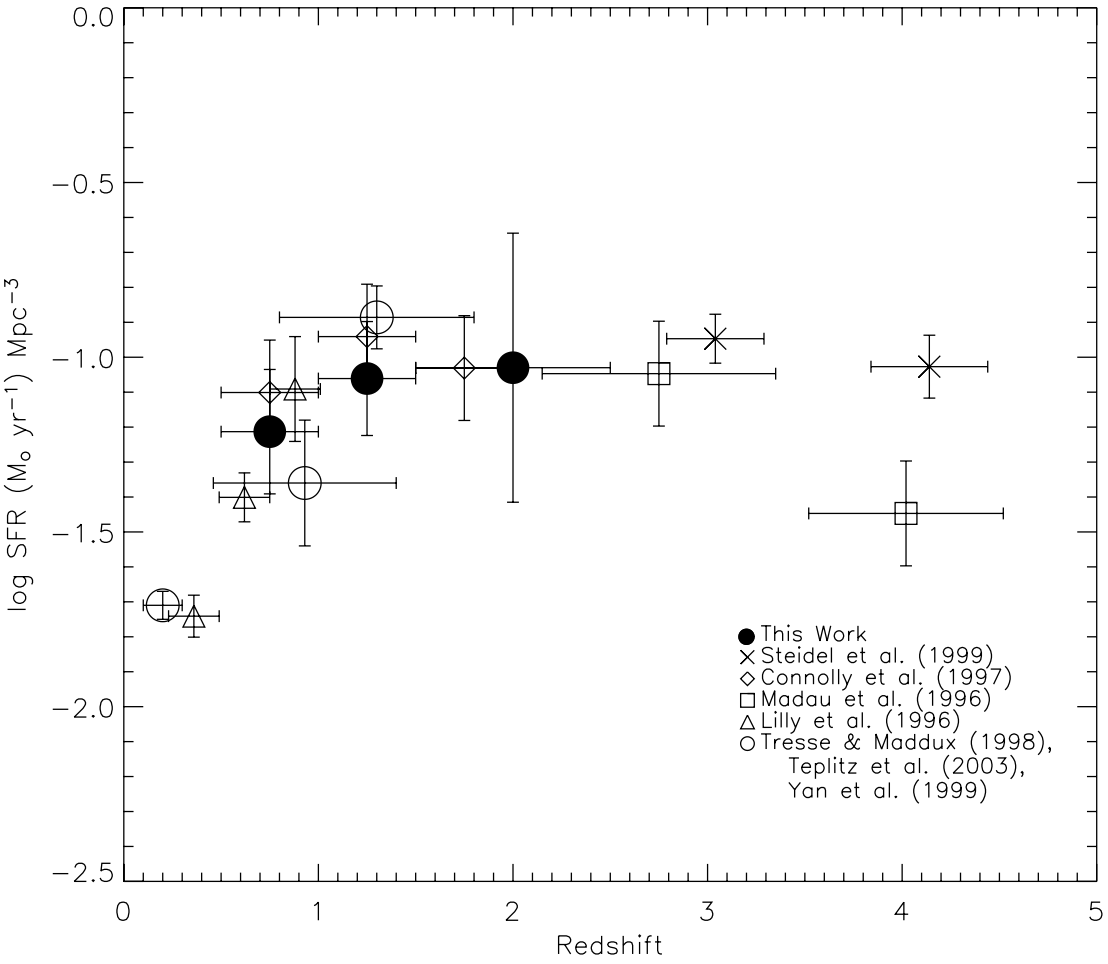

FIG. 12.—Extinction-corrected star formation history of the universe, where a Salpeter IMF has been used to translate δ_{2800} to $\delta_{\rm SFR}$. The solid circles are star formation rate densities from this study, open triangles are from Lilly et al. (1996), the open diamonds are from Connolly et al. (1997), the open squares from Madau et al. (1996), and the crosses are from Steidel et al. (1999). Also plotted, as open circles, are star formation rate densities determined from several different emission line (Hα and O II) studies (Tresse & Maddox 1998; Yan et al. 1999; Teplitz et al. 2003).

has a different shape than that of the typical field galaxy distribution. No differences were seen for evolved galaxies or integrated *R*-band luminosity density.

4.3. *Star Formation Rate*

While the near-infrared data are optimized to gain information about rest-wavelength optical flux from high-redshift galaxies, we also have information on rest-wavelength ultraviolet from our matching optical data set. In particular, we can measure the UV 2800 Å flux for our $z = 0.75$, 1.25, and 2 redshift bins, from which we can follow the formulation given by Madau et al. (1996) to determine the star formation rate density for the universe, if we assume a Salpeter initial mass function:

$$\rho_{\rm SFR} = 1.5 \times 10^{-28} \rho_{2800}\ M_\odot\ {\rm yr}^{-1}\ {\rm Mpc}^{-3}, \qquad (2)$$

where ρ_{2800} is given in ergs s^{-1} Hz^{-1} Mpc^{-3}. To determine ρ_{2800} we fit the ρ_{2800} luminosity function with a Schechter function before integrating over all magnitudes. The best-fit α at each redshift ranged from 0.13 to -0.75, significantly different than that assumed for most studies conducted near $z = 1$ (i.e., Lilly et al. 1996; Connolly et al. 1997; Yan et al. 1999), which typically find rising functions with α around -1.3. At higher redshift, Steidel et al. (1999) found that an $\alpha = -1.6$ fit their $z = 3$ luminosity function best. This difference may be a result of our near-infrared selection, which may miss significant numbers of ultraviolet sub-$L_\star$ galaxies, a result previously seen in the *K*-band–selected star formation rate measurements of Gabasch et al. (2004).

The main dilemma in reporting star formation rates from ultraviolet light is how much to correct for dust extinction. In principle, determinations of $E(B-V)$ determined using near-infrared data should be superior to those found from optical alone, as we understand the SEDs and dust extinction of the rest-wavelength optical much better than we do the rest-wavelength ultraviolet. Optical studies may also miss the most highly extincted objects, which in the nearby universe also tend to be those with the highest star formation rates. To examine this problem we ran our photometric fitting procedure with a Calzetti et al. (2000) dust extinction law and compared our results to those of Steidel et al. (1999), who used the Calzetti law to fit an $E(B-V)$ for 564 galaxies [median $E(B-V) \sim 0.15$]. The normalized $E(B-V)$ distributions are presented in Figure 11. Our fitting method did not allow for negative dust extinctions, so we placed all of the Steidel et al. (1999) galaxies with negative $E(B-V)$ values into the $E(B-V) = 0$–0.1 bin, adding roughly 50% to its counts. While not yet as well studied, the BX/BM galaxies appear to have approximately the same median $E(B-V)$ as their higher redshift Lyman break galaxy counterparts (Reddy et al. 2005).

There is a clear difference in the $E(B-V)$ distribution found between the optical/UV and near-infrared–selected samples, with

the near-infrared sample more extended to higher extinction. There is a substantial tail of near-infrared–selected sources with $E(B-V) > 0.4$, roughly 15% of the sample, compared to ~1% for the optical/UV-selection method. The median $E(B-V)$ across all redshift bins is 0.2, with slightly higher median values at the redshifts of the Bright Ages [$E(B-V) \sim 0.3$ from $z = 1$ to $z = 2.5$]. This is slightly bluer than the median reddening found for *BzK* [$E(B-V) \sim 0.4$; Daddi et al. 2004].

A Kolmogorov-Smirnov (K-S) test finds a highly significant difference between the Steidel et al. (1999) $z = 3$ sample and all of the near-infrared redshift samples. It would appear that our study is sensitive to a substantial population of more highly extincted galaxies missed by studies of Lyman break galaxies. It would also appear, at least from statistics of this study, that these missed galaxies will have only a modest impact on total light and star formation in the $z = 1$–2.5 Bright Ages. We attempted fitting extinctions higher than $E(B-V) = 0.5$, but generally found it degraded the quality of the photometric redshifts and did not seem to provide reliable extinction estimates for the most extincted galaxies. For some of these redder galaxies, the fitting would always select the maximum extinction available, no matter how large the allowable extinction had been set. From this we conclude that for some of the highest extincted galaxies, the fit value of $E(B-V)$ should probably be regarded as a lower limit.

To calculate a meaningful star formation rate density requires correction for this extinction. Continuing to use the Calzetti et al. (2000) law used in the Hyperz fits, we correct the UV 2800 Å flux of all galaxies in the sample with deep optical data, which excludes the 0149+336 field. To compare with other studies, we use a $q_0 = 0.5$, $H_0 = 50$ cosmology. To compare dust-extinction–corrected star formation rates, we applied the dust law to the data points from the other studies, using a value of $E(B-V) = 0.20$, the median value of our data.

The final result is plotted in Figure 12, with $\rho_{\rm SFR}(z = 0.5\text{–}1) = 0.061\ M_\odot\ {\rm yr}^{-1}\ {\rm Mpc}^{-3}$, $\rho_{\rm SFR}(z = 1\text{–}1.5) = 0.087\ M_\odot\ {\rm yr}^{-1}\ {\rm Mpc}^{-3}$ and $\rho_{\rm SFR}(z = 1.5\text{–}2.5) = 0.093\ M_\odot\ {\rm yr}^{-1}\ {\rm Mpc}^{-3}$. These near-infrared–selected points agree well with previous studies, most of which are optically selected, with only the $z = 1$–1.5 star formation density appearing to be low, although consistent within error bars. If *K*-selected studies do miss significant numbers of sub-$L_\star$ ultraviolet galaxies, then these star formation rate densities should probably be treated as lower limits, although corrections for steeper faint end slopes are unlikely to be more than a factor of 2. Alternatively, it should also be kept in mind that any contamination issues would lower these SFR densities. Unless a substantial amount of flux is hidden in faint galaxies, these SFR density measurements appear to be consistent with a relatively flat cosmic star formation rate from $z = 1$ to $z = 4$.

5. CONCLUSIONS AND FUTURE PROSPECTS

Many studies of the high-redshift universe have been undertaken in the rest-wavelength ultraviolet, potentially missing a significant population of red galaxies at high redshift. To address this concern, we construct a *K*-band–selected sample with photometric redshifts derived from multicolor photometry, reliable to an rms dispersion of $\sigma_z/(1+z) = 0.11$. *R*-band luminosity functions built from these photometric redshifts demonstrate that the period of time around $z = 2$ may be the epoch hosting the brightest galaxies in the history of our universe. There is marginal evidence for a factor of ~4 decrease in overall galaxy number density from $z = 0.5$ to $z = 2$. Evolved galaxies (E, S0, Sa) show a decreasing contribution to the total *R*-band luminosity density with redshift.

We have derived the star formation rate density for a near-infrared–selected sample out to $z = 2$. The agreement with previous studies indicates that both near-infrared and optical selection find similar quantities of star formation from both near-infrared and optical selection. However, as the star formation is derived from rest-wavelength ultraviolet flux, we could easily be missing any ultraviolet light absorbed by dust.

The greatest challenge in the determination of star formation at high redshift is assessing the impact of dust extinction on the derived star formation rate. Our examination of dust extinction for the near-infrared–selected sample of galaxies suggest a moderate increase in the number of dusty galaxies compared to optical searches. This does not, however, exclude a substantial population of galaxies so extincted as to be eliminated even from a near-infrared study.

K-band surveys at our depth and a real coverage (~80 arcmin^2) may soon be superseded by the next generation of large area surveys and detectors. In addition, deep mid-infrared surveys with the *Spitzer Space Telescope* should be able to produce samples unbiased by dust extinction to extremely high redshifts. Examination of the high-redshift universe is a significant component of its mission, with Legacy programs devoted to deep studies, like the Great Observatories Origins Deep Survey (GOODS). As high-redshift studies shift into the rest-wavelength near-infrared, a substantial population of dusty high-redshift galaxies will find little wavelength space in which to hide.

We thank the anonymous referee for their invaluable comments that improved this paper immensely. The authors would like to acknowledge the assistance of Rick Edelson, Andrew Fruchter, William Keel, Anuradha Koratkar, Jason Marshall, Roser Pello, Alice Shapley, Harry Teplitz, and Roger Windhorst, who all contributed some of their precious time to help with this work. We wish to thank the staff of the Keck observatories for their valuable help, particularly Paola Amico and all her aid with LRIS. Similarly, we must thank Micol Bolzonella, Joan-Marc Miralles, and Roser Pello for producing and publicly releasing their Hyperz photometric redshift code. The authors wish to recognize and acknowledge the very significant cultural role and reverence that the summit of Mauna Kea has always had within the indigenous Hawaiian community. We are most fortunate to have the opportunity to conduct observations from this mountain. Finally, the authors would like to acknowledge financial support from a grant for *HST* program AR-9543.

REFERENCES

Adelberger, K. L., & Steidel, C. C. 2000, ApJ, 544, 218
Adelberger, K. L., Steidel, C. C., Shapley, A. E., Hunt, M. P., Erb, D. K., Reddy, N. A., & Pettini, M. 2004, ApJ, 607, 226
Barmby, P., et al. 2004, ApJS, 154, 97
Benitez, N. 2000, ApJ, 536, 571
Bessell, M. S., Castelli, F., & Plez, B. 1998, A&A, 333, 231
Blanton, M. R., et al. 2001, AJ, 121, 2358
Bolzonella, M., Miralles, J.-M., & Pelló, R. 2000, A&A, 363, 476
Bruzual, G., & Charlot, S. 1993, ApJ, 405, 538
Calzetti, D. 1997, in AIP Conf. Proc.408, The Ultraviolet Universe at Low and High Redshift, ed. W. H. Waller (Melville: AIP), 403
Calzetti, D., Armus, L., Bohlin, R. C., Kinney, A. L., Koornneef, J., & Storchi-Bergmann, T. 2000, ApJ, 533, 682
Campos, A., Yahil, A., Windhorst, R. A., Richards, E. A., Pascarelle, S., Impey, C., & Petry, C. 1999, ApJ, 511, L1
Chapman, S. C., Blain, A. W., Smail, I., & Ivison, R. J. 2005, ApJ, 622, 772
Chen, H-W., et al. 2003, ApJ, 586, 745
Cimatti, A., et al. 2002a, A&A, 381, L68

Cimatti, A., et al. 2002b, A&A, 392, 395
———. 2002c, A&A, 391, L1
———. 2003, A&A, 412, L1
———. 2004, Nature, 430, 184
Cohen, J. G. 2002, ApJ, 567, 672
Cohen, J. G., Hogg, D. W., Blandford, R., Cowie, L. L., Hu, E., Songaila, A., Shopbell, P., & Richberg, K. 2000, ApJ, 538, 29
Colbert, J. W., Malkan, M. A., Rich, R. M., Frogel, J. A., Salim, S., & Teplitz, H. 2006, ApJ 638, 601 (Paper I)
Coleman, G. D., Wu, C. C., & Weedman, D. W. 1980, ApJS, 43, 393 (CWW80)
Connolly, A. J., Szalay, A. S., Dickinson, M., Subbarao, M. U., & Brunner, R. J. 1997, ApJ, 486, L11
Conselice, C. J., et al. 2004, ApJ, 600, L139
Cowie, L. L., Gardner, J. P., Hu, E. M., Songaila, A., Hodapp, K.-W., & Wainscoat, R. J. 1994, ApJ, 434, 114
Cross, N., et al. 2001, MNRAS, 324, 825
Daddi, E., Cimatti, A., Renzini, A., Fontana, A., Mignoli, M., Pozzetti, L., Tozzi, P., & Zamorani, G. 2004, ApJ, 617, 746
Dickinson, M. 1998, in The Hubble Deep Field, ed. M. Livio, S. M. Fall, & P. Madau (Cambridge: Cambridge Univ. Press), 219
Drory, N., Feulner, G., Bender, R., Botzler, C. S., Hopp, U., Maraston, C., Mendes de Oliveira, C., & Snigula, J. 2001, MNRAS, 325, 550
Elbaz, D., Cesarsky, C. J., Chanial, P., Aussel, H., Franceschini, A., Fadda, D., & Chary, R. R. 2002, A&A, 384, 848
Felten, J. E. 1977, AJ, 82, 861
Fernandez-Soto, A. Lanzetta, K. M., Chen, H-W., Pascarelle, S. M., & Yahata, N. 2001, ApJS, 135, 41
Fioc, M., & Rocca-Volmerange, B. 1997, A&A, 326, 950
Firth, A. E., et al. 2002, MNRAS, 332, 617
Folkes, S., et al. 1999, MNRAS, 308, 459
Förster Schreiber, N. M., et al. 2004, ApJ, 616, 40
Franx, M., et al. 2000, Messenger, 99, 20
———. 2003, ApJ, 587, L79
Gabasch, A., et al. 2004, ApJ, 616, L83
Giallongo, E., Salimbeni, S., Menci, N., Zamorani, G., Fontana, A., Dickinson, M., Cristiani, S., & Pozzetti, L. 2005, ApJ, 622, 116
Giavalisco, M., Steidel, C. C., & Macchetto, F. D. 1996, ApJ, 470, 189
Giavalisco, M., et al. 2004, ApJ, 600, L103
González Delgado, R. M., Heckman, T., Leitherer, C., Meurer, G., Krolik, J., Wilson, A. S., Kinney, A., & Koratkar, A. 1998, ApJ, 505, 174
Kashikawa, N., et al. 2003, AJ, 125, 53
Keel, W. C., Cohen, S. H., Windhorst, R. A., & Waddington, I. 1999, AJ, 118, 2547
Kinney, A. L., Calzetti, D., Bohlin, R. C., McQuade, K., Storchi-Bergmann, T., & Schmitt, H. R. 1996, ApJ, 467, 38
Labbé, I., et al. 2005, ApJ, 624, L81
Le Borgne, D., & Rocca-Volmerange, B. 2002, A&A, 386, 446
Lilly, S. J., Le Fevre, O., Hammer, F., & Crampton, D. 1996, ApJ, 460, L1
Lilly, S. J., Tresse, L., Hammer, F., Crampton, D., & Le Fevre, O. 1995, ApJ, 455, 108
Lin, H., Kirshner, R. P., Shectman, S. A., Landy, S. D., Oemler, A., Tucker, D. L., & Schechter, P. L. 1996, ApJ, 464, 60
Lin, H., Yee, H. K. C., Carlberg, R. G., Morris, S. L., Sawicki, M., Patton, D. R., Wirth, G., & Shepherd, C. W. 1999, ApJ, 518, 533
Madau, P., Ferguson, H. C., Dickinson, M. E., Giavalisco, M., Steidel, C. C., & Fruchter, A. 1996, MNRAS, 283, 1388
Malkan, M. A., & Stecker, F. W. 2001, ApJ, 555, 641
Malkan, M. A., Teplitz, H., & McLean, I. S. 1996, ApJ, 468, L9
Martin, D. C., et al. 2005, ApJ, 619, L59
McCarthy, P. J., et al. 2001, ApJ, 560, L131
McLeod, B. A., Bernstein, G. M., Rieke, M. J., Tollestrup, E. V., & Fazio, G. G. 1995, ApJS, 96, 117
Oke, J. B., et al. 1995, PASP, 107, 375
Palunas, P., Teplitz, H. I., Francis, P. J., Williger, G. M., & Woodgate, B. E. 2004, ApJ, 602, 545
Pascarelle, S. M., Windhorst, R. A., & Keel, W. C. 1998, AJ, 116, 2659
Pascarelle, S. M., Windhorst, R. A., Keel, W. C., & Odewahn, S. C. 1996, Nature, 383, 45
Pozzetti, L., & Mannucci, F. 2000, MNRAS, 317, L17
Pozzetti, L., et al. 2003, A&A, 402, 837
Reddy, N. A., Erb, D. K., Steidel, C. C., Shapley, A. E., Adelberger, K. L., & Pettini, M. 2005, ApJ, 633, 748
———. 2005, AJ, 129, 1183
Rudnick, G., et al. 2001, AJ, 122, 2205
Shapley, A. E., Steidel, C. C., Adelberger, K. L., Dickinson, M., Giavalisco, M., & Pettini, M. 2001, ApJ, 562, 95
Shapley, A. E., Steidel, C. C., Erb, D. K., Reddy, N. A., Adelberger, K. L., Pettini, M., Barmby, P., & Huang, J. 2005, ApJ, 626, 698
Shapley, A. E., Steidel, C. C., Pettini, M., & Adelberger, K. L. 2003, ApJ, 588, 65
Smail, I., Ivison, R. J., Blain, A. W., & Kneib, J.-P. 2002, MNRAS, 331, 495
Somerville, R. S., Lee, K., Ferguson, H. C., Gardner, J. P., Moustakas, L. A., & Giavalisco, M. 2004, ApJ, 600, L171
Spinoglio, L., Malkan, M. A., Rush, B., Carrasco, L., & Recillas-Cruz, E. 1995, ApJ, 453, 616
Steidel, C. C., Adelberger, K. L, Giavalisco, M., Dickinson, M., & Pettini, M. 1999, ApJ, 519, 1
Steidel, C. C., & Hamilton, D. 1993, AJ, 105, 2017
Steidel, C. C., Shapley, A. E., Pettini, M., Adelberger, K. L., Erb, D. K., Reddy, N. A., & Hunt, M. P. 2004, ApJ, 604, 534
Storchi-Bergmann, T., Calzetti, D., & Kinney, A. L. 1998, Database of UV-Optical Spectra of Nearby Quiescent and Active Galaxies (Baltimore: STSci), http://www.stsci.edu/ftp/catalogs/nearby_gal/sed.html
Teplitz, H. I., Collins, N. R., Gardner, J. P., Hill, R. S., & Rhodes, J. 2003, ApJ, 589, 704
Tresse, L., & Maddox, S. J. 1998, ApJ, 495, 691
van Dokkum, P. G., et al. 2003, ApJ, 587, L83
Yan, L., McCarthy, P. J., Freudling, W., Teplitz, H. I., Malumuth, E. M., Weymann, R. J., & Malkan, M. A. 1999, ApJ, 519, L47
York, D. G., et al. 2000, AJ, 120, 1579